

UNIVERSITY OF OKLAHOMA  
GRADUATE COLLEGE

A GEOMETRY MODELING AND OPTIMIZATION PIPELINE FOR THE  
ATRIOVENTRICULAR HEART VALVES

A THESIS  
SUBMITTED TO THE GRADUATE FACULTY  
in partial fulfillment of the requirements for the  
Degree of  
MASTER OF SCIENCE

By  
LUKE CHARLES WHITNEY  
Norman, Oklahoma  
2023

A GEOMETRY MODELING AND OPTIMIZATION PIPELINE FOR THE  
ATRIOVENTRICULAR HEART VALVES

A THESIS APPROVED FOR THE  
SCHOOL OF AEROSPACE AND MECHANICAL ENGINEERING

BY THE COMMITTEE CONSISTING OF

Dr. Chung-Hao Lee, Chair

Dr. Kuang-Hua Chang

Dr. Chenkai Dai

© Copyright by LUKE WHITNEY 2023

All Rights Reserved.

## **ACKNOWLEDGMENTS**

I would like to thank my friends and family, and especially my wife Madelyn, for their continued support while I completed this thesis. I would also like to thank my advisor, Dr. Chung-Hao Lee, for his part in helping me grow both as a student and as an individual.

# ABSTRACT OF THE THESIS

A GEOMETRY MODELING AND OPTIMIZATION PIPELINE FOR THE  
ATRIOVENTRICULAR HEART VALVES

by

Luke Charles Whitney

Master of Science in Mechanical Engineering

University of Oklahoma, Norman, OK, 2023

Dr. Chung-Hao Lee, Chair

The objective of this research is to develop a pipeline for modeling the tricuspid heart valve that can be used as an adaptable tool for furthering research in the field, including treatment options for heart valve disease such as functional tricuspid regurgitation. We first gathered data from micro-computed tomography scans of porcine heart valves to extract the valve shape and identify the annulus. The data were transformed and sent to a computer-aided design (CAD) modeling software in a streamlined process. We then combined the initial shape of the valve with a set of input parameters to define a leaflet surface using non-uniform rational B-splines (NURBS). Additional NURBS curves were further defined to create beam elements modeling the valve chordae tendineae. The resulting CAD model was used to rep-

resent the valve's shape, which we provide four examples of using different input data sets. The model's adaptability was demonstrated with additional examples using mitral valve data. We also combined the model with a non-linear isotropic constitutive model for the leaflets to directly use isogeometric analysis to evaluate the closure of the valve. This valve model creation, using only a set of initial data and input parameters, was combined with a genetic algorithm search pattern to demonstrate optimization capabilities of the modeling pipeline. The pipeline was used to minimize an objective function for the coaptation area of the valve model, which affects the quality of the valve's closure and reduces chances of tricuspid regurgitation. Additionally, the generated CAD model was printed using rapid prototyping to create a physical version of the model that can be used for patient education in a clinical setting. The presented modeling pipeline provides the next step in streamlining the process from data acquisition to improving biomechanical understanding of the tricuspid valve, bridging the research gap currently present with the tricuspid valve.

# CONTENTS

<b>List of Figures</b>	<b>xi</b>
<b>List of Tables</b>	<b>xii</b>
<b>List of Symbols</b>	<b>xii</b>
<b>List of Abbreviations</b>	<b>xiii</b>
<b>1 Introduction</b>	<b>1</b>
1.1 Motivation . . . . .	1
1.2 Objective and Scope . . . . .	2
<b>2 Literature Review</b>	<b>4</b>
2.1 Tricuspid Valve Anatomy . . . . .	4
2.2 Modeling of the Tricuspid Valve . . . . .	8
2.3 Tricuspid Regurgitation . . . . .	14
<b>3 Geometry Modeling Pipeline</b>	<b>19</b>
3.1 Digitizing Heart Valve Surfaces . . . . .	20
3.2 Rhinoceros and Grasshopper . . . . .	22
<b>4 Geometry Modeling Examples</b>	<b>33</b>
4.1 Tricuspid Valve Geometries . . . . .	33
4.2 Adaptability of the TV Model . . . . .	41
4.3 Application to the study of the Mitral Valve . . . . .	43

<b>5</b>	<b>Modeling Applications</b>	<b>49</b>
5.1	Isogeometric Analysis . . . . .	49
5.2	Optimization . . . . .	51
5.3	Patient Education . . . . .	55
<b>6</b>	<b>Conclusions and Future Work</b>	<b>60</b>
6.1	Conclusions . . . . .	60
6.1.1	Geometry Modeling Pipeline . . . . .	61
6.1.2	Modeling Applications . . . . .	61
6.2	Recommendations for Future Research . . . . .	61
6.2.1	Additional patient-specific parameters . . . . .	61
6.2.2	Streamlining valve segmentation . . . . .	62
6.2.3	Dynamic modeling conditions . . . . .	62
6.2.4	Alternate optimization methods . . . . .	63
	<b>References</b>	<b>64</b>



## LIST OF FIGURES

Fig. 2.1	TV location in the right heart . . . . .	5
Fig. 2.2	An excised porcine tricuspid valve . . . . .	5
Fig. 2.3	Annulus saddle shape . . . . .	8
Fig. 2.4	Chordae tendineae dissection . . . . .	9
Fig. 2.5	Tricuspid model used in Stevanella <i>et al.</i> . . . . .	9
Fig. 2.6	Tricuspid model used in Aversa and Careddu . . . . .	10
Fig. 2.7	Singh-Gryzbon <i>et al.</i> tricuspid model . . . . .	12
Fig. 2.8	Comparison of manual and multi-atlas segmentation for three patient TVs . . . . .	13
Fig. 2.9	A depiction of Ebstein’s anomaly . . . . .	15
Fig. 2.10	Functional tricuspid regurgitation . . . . .	16
Fig. 2.11	Publications and citations related to the four heart valves since 1990 . . . . .	17
Fig. 2.12	Imaging of an infant patient with pulmonary atresia . . . . .	17
Fig. 2.13	Annuloplasty ring . . . . .	18
Fig. 3.1	TV surface mapped in GrabIt . . . . .	21
Fig. 3.2	TV point cloud generated in MATLAB . . . . .	22
Fig. 3.3	TV point cloud with annulus points . . . . .	23
Fig. 3.4	Annulus points with curve interpolation. . . . .	24
Fig. 3.5	Rebuilt annulus NURBS curve with control polygon . . . . .	24

Fig. 3.6 Labeled parameter heights used for the tricuspid valve model . . . . .	25
Fig. 3.7 Leaflet and commissure locations along the annulus curve.	25
Fig. 3.8 Leaflet and commissure heights offset from the annulus.	26
Fig. 3.9 Interpolated leaflet free edge. . . . .	27
Fig. 3.10 Control points for leaflet surface. . . . .	27
Fig. 3.11 Gordon surface created using the annulus and free edge curves and six leaflet height curves. . . . .	28
Fig. 3.12 TV model superimposed with $\mu$ CT scan . . . . .	29
Fig. 3.13 Straight chordae limitation . . . . .	30
Fig. 3.14 Four three-strand chordae groups added to the TV leaflet surface model. . . . .	31
Fig. 3.15 Completed tricuspid valve (TV) model. . . . .	32
Fig. 3.16 Overview of the developed TV model pipeline . . . . .	32
Fig. 4.1 TV-1 leaflet surface fitting . . . . .	35
Fig. 4.2 TV-2 leaflet surface fitting . . . . .	36
Fig. 4.3 TV-3 and its $\mu$ CT scan . . . . .	37
Fig. 4.4 TV-3 $\mu$ CT scan with highlighted leaflets . . . . .	37
Fig. 4.5 Transformed surface point cloud for TV-3 . . . . .	38
Fig. 4.6 TV-3 annulus curve fit with leaflet and commissure locations	39
Fig. 4.7 TV-3 valve surface fit with leaflet and commissure heights	39
Fig. 4.8 Final TV-3 model . . . . .	39
Fig. 4.9 TV-4 leaflet surface fitting . . . . .	40
Fig. 4.10 Fixed TV-4 sample . . . . .	41
Fig. 4.11 Different parameter heights for the same annulus data . .	42
Fig. 4.12 Different chordae configurations for the same leaflet surface and papillary muscle positions . . . . .	43
Fig. 4.13 MV leaflet measurements . . . . .	45
Fig. 4.14 Point clouds for mitral valves . . . . .	46

Fig. 4.15 MV01 point cloud in Rhino . . . . .	47
Fig. 4.16 MV01 point cloud and model . . . . .	48
Fig. 5.1 Closed TV configuration . . . . .	52
Fig. 5.2 Optimization framework . . . . .	54
Fig. 5.3 Objective function value as optimization continues. . . . .	55
Fig. 5.4 Best TV configuration, undeformed and deformed . . . . .	56
Fig. 5.5 Best TV configuration with maximum in-plane Green-Lagrange strain . . . . .	56
Fig. 5.6 An overview of the full optimization pipeline. . . . .	57
Fig. 5.7 3D-printed TV leaflet surface. . . . .	58
Fig. 5.8 3D-printed TV closed leaflet surface. . . . .	59

## LIST OF TABLES

Table 2.1	Tricuspid valve measurements . . . . .	7
Table 4.1	Sample TV leaflet and commissure heights . . . . .	34
Table 4.2	Mitral valve measurements . . . . .	44

## LIST OF ABBREVIATIONS

<b><math>\mu</math>CT</b>	micro-computed tomography . . . . .	2
<b>2DTTE</b>	two-dimensional transthoracic echocardiography . . . . .	16
<b>AV</b>	aortic valve . . . . .	2
<b>CAD</b>	computer-aided design . . . . .	v
<b>CT</b>	computed tomography . . . . .	11
<b>FE</b>	finite element . . . . .	11
<b>FSI</b>	fluid-structure interaction . . . . .	11
<b>IGA</b>	isogeometric analysis . . . . .	14
<b>MIPE</b>	maximum in-plane Green-Lagrange strain . . . . .	55
<b>MRI</b>	magnetic resonance imaging . . . . .	16
<b>MV</b>	mitral valve . . . . .	1
<b>NURBS</b>	non-uniform rational B-splines . . . . .	v
<b>PLA</b>	polylactic acid . . . . .	58
<b>TR</b>	tricuspid regurgitation . . . . .	1
<b>TV</b>	tricuspid valve . . . . .	x

*Note for electronic copy: All figures, tables, equations, references, and items included in the Table of Contents and Lists are hyperlinked. For example, acronyms in the document have backward links to the List of Abbreviations to facilitate the reader's understanding. To maintain readability, these links are not highlighted. Instead, the cursor transforms into a pointing hand when hovering over a linked item.*

# 1 INTRODUCTION

1.1 Motivation . . . . .	1
1.2 Objective and Scope . . . . .	2

## 1.1 Motivation

The TV is an essential component of the heart that regulates proper blood flow from the right atrium to the right ventricle. When the heart relaxes during diastole, the tricuspid valve opens to allow blood to flow forward from the atrium to the ventricle, and when the heart contracts during systole, the tricuspid valve closes to prevent this blood from flowing back into the atrium. However, changes in the shape of the heart or TV can prevent the valve from closing properly, resulting in blood back flow known as tricuspid regurgitation (TR). This regurgitant flow of blood gradually creates an overload in the heart which causes remodeling in the heart tissue and can eventually lead to heart failure. To remedy this, proper surgical intervention is required, and this relies on a solid understanding of how the TV functions under various diseased and surgically intervened conditions.

Of the four heart valves, the tricuspid valve has received the least attention in research, with far more attention being given to the mitral valve (MV)

and aortic valve (AV) of the left side of the heart, leading to its label of “the forgotten valve.”<sup>[1,2]</sup> This is partly because surgeons and cardiologists long believed that functional tricuspid regurgitation would regress naturally after surgical repair of mitral valve disease on the left side of the heart. In 2005, however, Dreyfus *et al.* found that this is not the case, and that TR would progress to more severe stages despite MV surgery.<sup>[1]</sup> Research into the TV has improved dramatically since this study but is still far behind those established works of the mitral or aortic valve.

## 1.2 Objective and Scope

The objective of this research is to develop a pipeline for modeling the tricuspid heart valve that can be used as an adaptable tool for furthering research in the field. This research can then better inform researchers and clinicians on possible outcomes to various treatment options for heart valve disease such as functional tricuspid regurgitation. We first gather data from micro-computed tomography ( $\mu$ CT) scans of porcine heart valves to extract the 3D shape of the valve. The data are transformed and sent to a CAD modeling software in a streamlined process. We then combine the initial shape of the valve with a set of input parameters to define a leaflet surface using NURBS. Additional NURBS curves are defined to create beam elements modeling the valve chordae tendineae. The resulting CAD model is used to represent the valve’s shape, which we give several examples of using different input data sets. We also use the model directly with isogeometric analysis to evaluate the closure of the valve. This is combined with a genetic algorithm search pattern to demonstrate optimization capabilities of the modeling pipeline. Additionally, the generated CAD model is printed using rapid prototyping to create a physical version of the model that can be used for patient education in a clinical setting.



The remainder of the thesis is organized as follows. Chapter 2 presents a literature review of prior research into the TV, including its anatomy and function, computational modeling, and functional tricuspid regurgitation. Chapter 3 lays out the components of the developed modeling pipeline in a piece-by-piece manner to show the overall procedure. Chapter 4 gives several examples of TV models created using the modeling pipeline to demonstrate its capabilities. Chapter 5 presents some applications for the modeling pipeline. Finally, Chapter 6 provides concluding remarks and suggests future extensions.

## 2 LITERATURE REVIEW

2.1 Tricuspid Valve Anatomy . . . . .	4
2.2 Modeling of the Tricuspid Valve . . . . .	8
2.3 Tricuspid Regurgitation . . . . .	14

### 2.1 Tricuspid Valve Anatomy

The TV is one of the two heart valves known as the atrioventricular valves due to its location between the right atrium and right ventricle of the heart (Fig. 2.1); the other being the MV on the left side of the heart. It regulates uni-directional blood flow from the right atrium to the right ventricle through the opening and closing of three leaflets, or cusps.

These three leaflets, the anterior, posterior and septal leaflets, are attached to the right atrium by a ring-like fibrous annulus. The TV leaflets consist of a single continuous tissue that is naturally separated into the leaflets by shorter sections of the tissue known as commissures. The free edge of the leaflets attaches to the papillary muscles in the right ventricle through the fibrous cords of tissue known as chordae tendineae. Figure 2.2 provides a labeled diagram of the valve's anatomy.

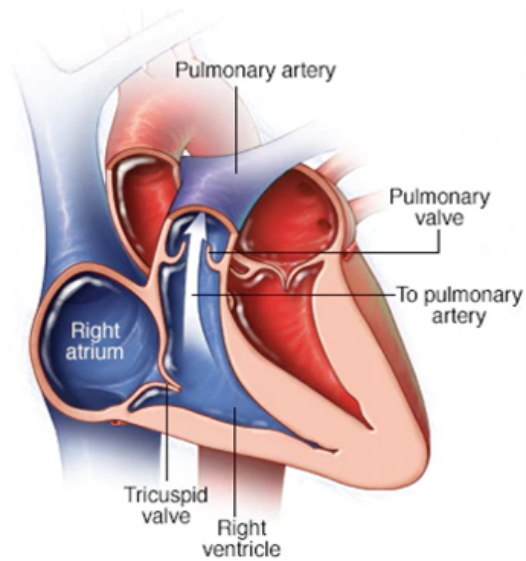


FIG. 2.1 TV location in the right heart. Image adapted from mayoclinic.org

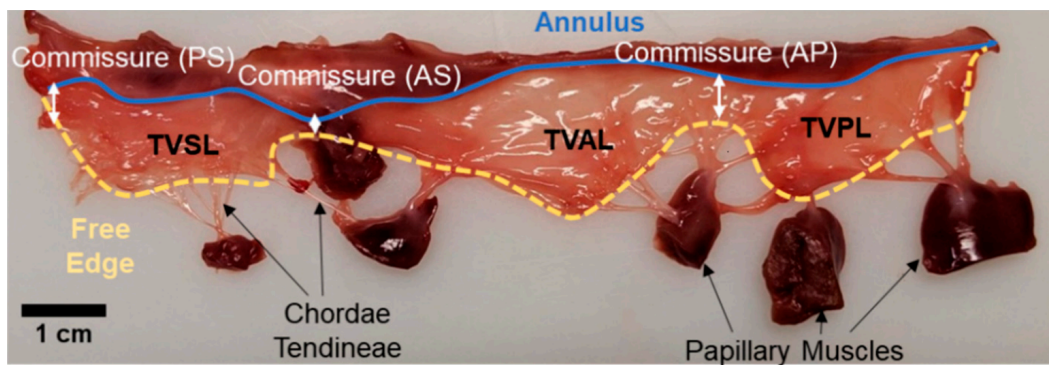


FIG. 2.2 An excised porcine TV showing the three leaflets and three commissures, annulus, chordae tendineae, and papillary muscles. Leaflets are labeled as anterior (AL), posterior (PL) and septal (SL), commissures are labeled as posteroseptal (PS), anteroseptal (AS), and anteroposterior (AP). From Lee *et al.*

The leaflets of the TV open into the ventricle during diastole, the relaxing stage of the heart, and then close during systole to prevent blood from flowing backward from the ventricle into the atrium as the heart contracts. Leaflet thickness is known to vary between leaflets in the TV. Khoiy *et al.*<sup>[4]</sup> found in their 2016 paper that the anterior and posterior leaflets had similar thicknesses ( $0.313 \pm 0.068$  mm and  $0.346 \pm 0.061$  mm, respectively), but the septal leaflet was significantly thicker ( $0.491 \pm 0.049$  mm) and had a lower standard deviation in thickness. Stevanella *et al.*<sup>[2]</sup> included detailed measurements of five human TVs and twenty porcine TVs when conducting their 2010 study on the TV, the results of which are included in Table 2.1. In their study, there was no significant difference in leaflet thickness between porcine and human specimens. They found the anterior leaflet to exhibit the largest height, followed by similar heights in the posterior and septal leaflets.

Hiro *et al.*<sup>[5]</sup> first attempted to characterize the TV annulus in sheep by placing sonometric crystals at certain locations on the valve leaflets and tracking the distances between them through the cardiac cycle. Using a least-squares regression of the crystal coordinates, they determined the plane of the annulus. They found the annulus to be saddle-shaped and to vary in size significantly during the cardiac cycle, expanding  $28.6 \pm 3.6\%$  in annular area and changing its shape from elliptical at the minimum area to circular at the maximum area. This study also tracked the locations of the papillary muscles and confirmed that the valve's opening and closing is not just a response to pressure change but could be due to annulus contraction and papillary muscle motion.<sup>[5,6]</sup> Another study by Fukuda *et al.*<sup>[7]</sup> confirmed the saddle-like shape of the TV annulus in humans by studying real-time 3D echocardiography imaging in fifteen healthy human patients. The high points of the saddle shape occur between the anterior and posterior leaflets and between the anterior and septal leaflets. Their study also

TABLE 2.1 TV measurements from Stevanella *et al.*

Dimension (mm)	Leaflet	Porcine	Human
Annulus length	Anterior	46.57 ± 8.53	40.00 ± 6.71
	Posterior	39.15 ± 9.00	32.04 ± 5.71
	Septal	34.21 ± 7.55	28.94 ± 5.40
Thickness	Anterior	0.390 ± 0.102	0.396 ± 0.101
	Posterior	0.378 ± 0.106	0.380 ± 0.086
	Septal	0.379 ± 0.105	0.413 ± 0.079
Leaflet height	Anterior	19.93 ± 3.53	24.96 ± 3.12
	Posterior	18.82 ± 3.22	21.54 ± 5.31
	Septal	18.62 ± 4.08	21.40 ± 2.69
Commissure height	Anterior	7.80 ± 2.02	11.16 ± 1.49
	Posterior	6.73 ± 1.58	13.36 ± 2.16
	Septal	6.69 ± 1.36	13.25 ± 2.22

showed the annulus to maintain this saddle shape (Fig. 2.3) throughout the cardiac cycle.

The chordae tendineae are complex, branching structures which prevent the valve from prolapsing into the atrium during systole (contracting of the heart). Silver *et al.*<sup>[8]</sup> first characterized the chordae tendineae in their 1971 study aiming to identify the morphology of the TV. This study created the classification system for the chordae. In addition to the three types of chordae found in the mitral valve, fan-shaped, rough zone, and basal, their study classified two additional chordae types unique to the TV: free-edge and deep chordae. A more recent work by Pokutta-Paskaleva *et al.*<sup>[9]</sup> studying porcine mitral and TVs categorized chordae as either strut, marginal or basal chordae. The two thickest chordae for each leaflet are identified as the strut chordae, though no strut chordae were identified for the septal

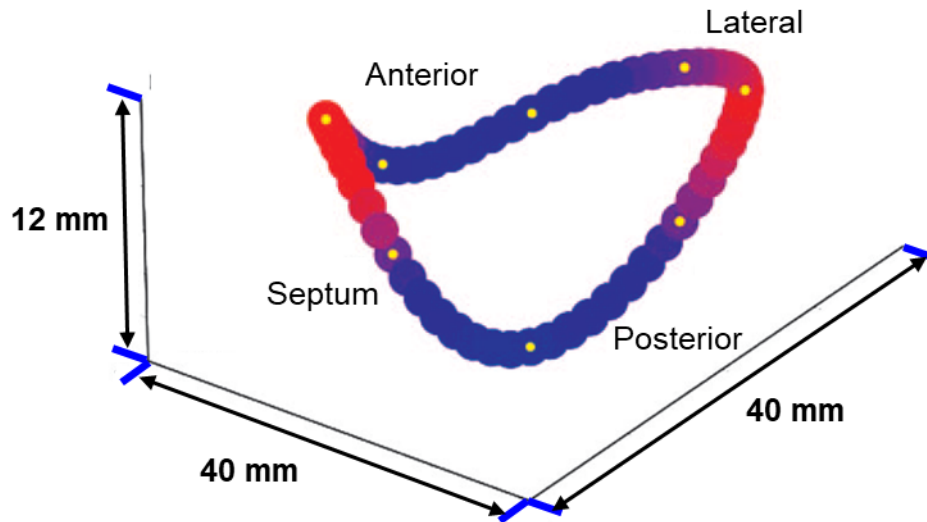
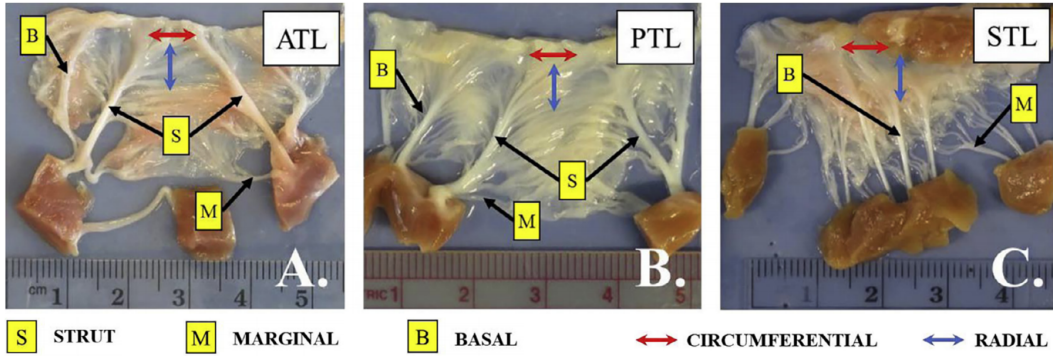


FIG. 2.3 Annulus saddle shape. Adapted from Fukuda *et al.*<sup>[7]</sup>

leaflet; their classification can be seen in Fig. 2.4. The marginal chordae attach along the free edge and the basal chordae attach further from the edge. For the TV, the strut chordae were thicker, with no difference between the marginal and basal thickness, and there was no difference in chordal thickness among the different leaflets.

## 2.2 Modeling of the Tricuspid Valve

Stevanella *et al.*<sup>[2]</sup> created the first finite element model of the TV, documented in their 2010 paper, paving the way for future finite element TV models. They used the annulus and papillary muscle location data collected by Hiro *et al.*<sup>[5]</sup> and their own set of leaflet measurements from both porcine and human TVs to construct a three-dimensional geometric model from cubic splines with chordae that were modeled as constant-thickness non-branched strings (Fig. 2.5). The leaflet surface used 40,300 three-node triangular plane-stress shell elements with a shear stiffness of



**FIG. 2.4** Chordae tendineae dissection. Adapted from Pokutta-Paskaleva *et al.*<sup>[9]</sup> (ATL: anterior tricuspid leaflet, PTL: posterior tricuspid leaflet, STL: septal tricuspid leaflet).

22 kPa and a uniform 0.396 mm thickness. They represented the chordae as non-branched strings with constant  $0.171 \text{ mm}^2$  cross sections. Comparisons of porcine and human dimensions suggested that the geometries are not in perfect agreement, with measurements indicating that human TVs are more elongated with more deformation than porcine TVs.<sup>[2]</sup> Stevanella *et al.*<sup>[2]</sup> applied the same pressure loading from Hiro *et al.*<sup>[5]</sup> to their model but compared their findings to mitral valve data since no studies on the biomechanical properties of the TV were available.

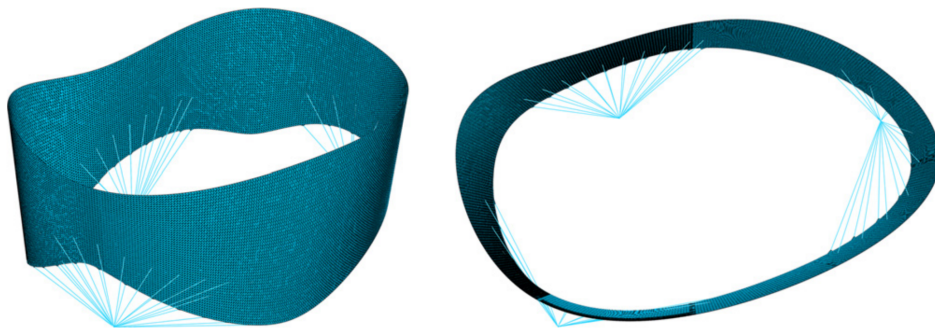


**FIG. 2.5** Tricuspid model used in Stevanella *et al.*

In their 2017 work, Aversa and Careddu<sup>[10]</sup> described the computational model from Stevanella *et al.* as the reference in the field, but they also pointed out that the approximations used affect the reliability of the

model. In particular, the model is limited by combining *ex vivo* human and porcine data and *in vivo* ovine data and by the lack of a characterization of the microstructure of the TV, since only mitral valve microstructure data was available. Aversa and Careddu<sup>[10]</sup> attempted to provide an improved model by integrating *in vitro* imaging in the form of 3D echocardiography with finite element modeling. From their collected data, they identified the commissure positions by measuring three local minima in the free edge of the leaflet at  $120 \pm 30$  degrees from one another. Their model used the chordae pattern data from Stevanella *et al.*<sup>[2]</sup> with the same constant cross-sectional area for the truss elements and the ovine papillary muscle location data from Hiro *et al.*<sup>[5]</sup> that was scaled to match their porcine data. They created a mesh for the leaflets using three-node triangular plane-stress shell elements. Their model and results are shown in Fig. 2.6. Valve closure was simulated by applying a time-dependent pressure traction on the ventricular surface, peaking at 23.7 mmHg. They also contracted the annulus according to the data found in Hiro *et al.*, though they kept papillary muscles stationary.

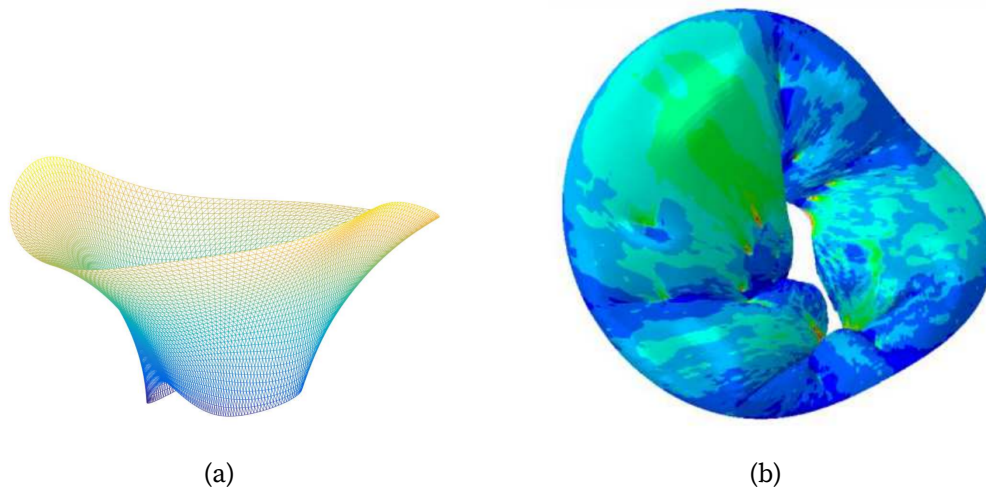


**FIG. 2.6** (a) Tricuspid leaflet mesh used in Aversa *et al.*<sup>[10]</sup> and (b) the closed surface with maximum in-plane principal stress.



Later, Kong *et al.*<sup>[11]</sup> attempted to improve upon the Stevanella *et al.* model by producing finite element models with patient-specific geometries. They segmented the TV from multi-slice computed tomography (CT) scans of the heart to obtain its geometry for multiple patients. Due to limited image quality, they were unable to obtain measurements for chordae locations and leaflet thickness, so values from literature and *ex vivo* measurements were used. Kong *et al.*<sup>[11]</sup> determined their valve configuration by iteratively adjusting the chordal lengths until the closed model geometry most closely matched the CT image geometry, keeping all the chordal attachments constant during these adjustments. Although it was limited by resolution and required manual segmentation, the model from Kong *et al.* was the first patient-specific finite element model of the TV, and it yielded good closing behavior of the leaflets.

To avoid approximating leaflet thickness and chordae dimensions, as was necessary in the work by Kong *et al.*, Singh-Gryzbon *et al.*<sup>[12]</sup> used high-resolution  $\mu$ CT images of an excised porcine TV to develop a fluid–structure interaction (FSI) model of the TV. The papillary muscles were affixed to movable rods that allowed adjustments of the papillary muscle position to generate normal leaflet coaptation for imaging. Their model is shown in Fig. 2.7. Despite the high resolution of the  $\mu$ CT images, some chordae were lost during the meshing step and had to be reconstructed manually. Their study found that structural finite element (FE)-only models are adequate for static configurations of heart valves but concluded that FSI is required to capture valve dynamics.

Pouch *et al.*<sup>[13]</sup> took transthoracic 3D echocardiography images of the TV and used multi-atlas label fusion to semi-automatically segment the TV geometry for studying hypoplastic left heart syndrome. They also used manual segmentation to compare to the semi-automated process. Some of these results can be seen in Fig. 2.8. They observed no significant difference between the two except for measurement of the septal leaflet’s surface area.

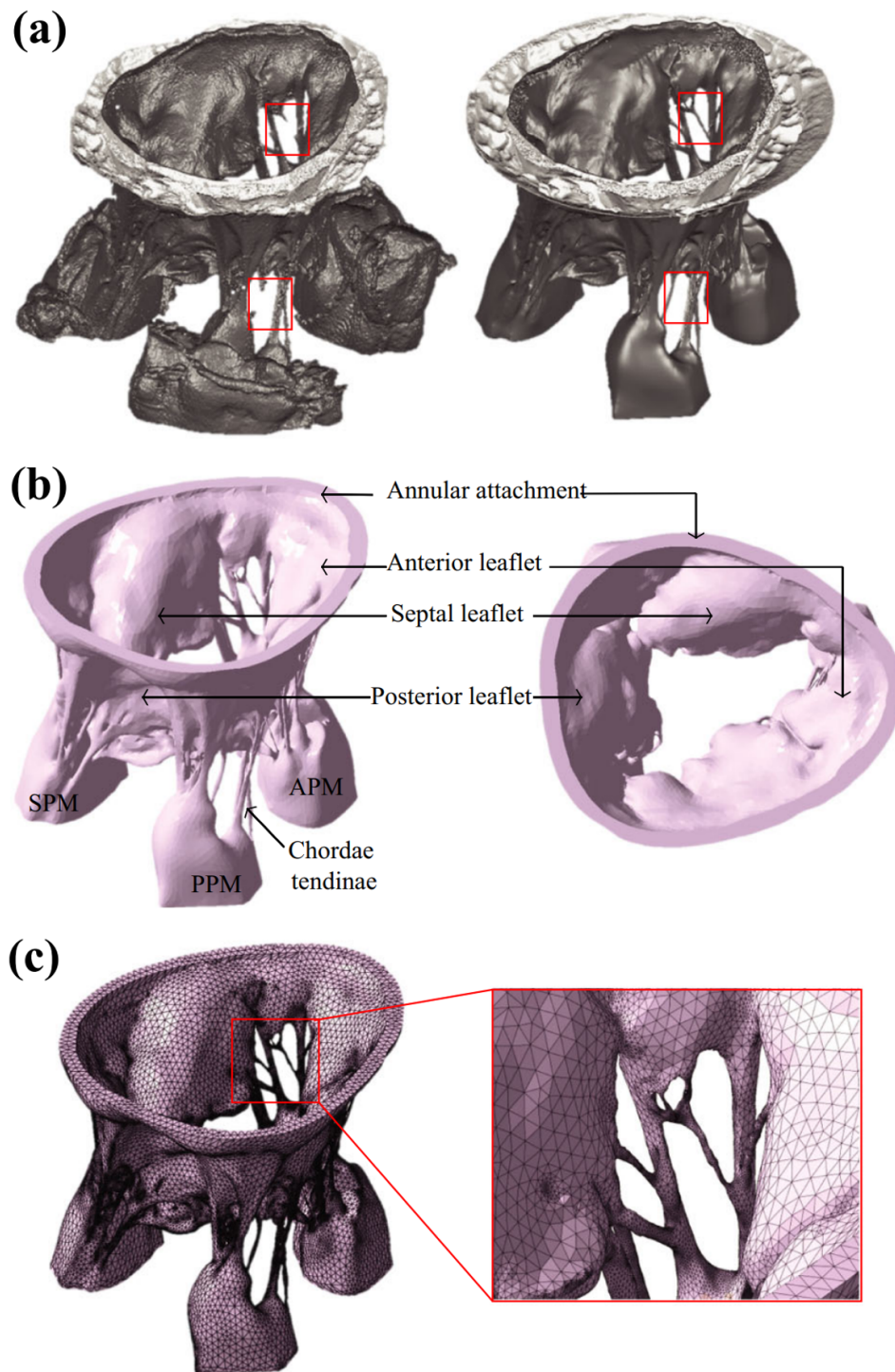


**FIG. 2.7** (a) Segmented  $\mu$ CT TV scan, (b) model, and (c) mesh used by Singh-Gryzbon *et al.*<sup>[12]</sup> Red boxes are areas where chordae had to be manually reconstructed.

They noted that manual segmentation is valuable for qualitative assessment, but that it does not automatically generate optimal visualizations. Pouch *et al.*<sup>[13]</sup> focused on segmentation for model creation and did not perform analysis with their models.

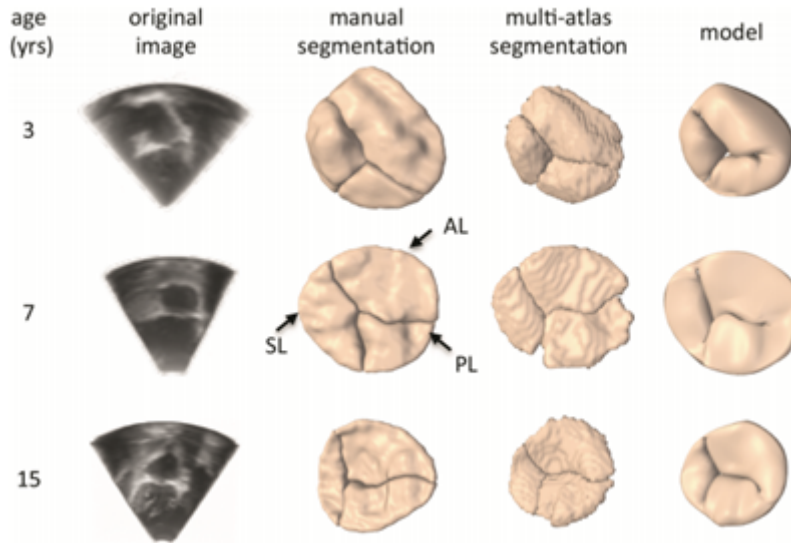


**FIG. 2.8** Comparison of manual and multi-atlas segmentation for three patient TVs. Adapted from Pouch *et al.*<sup>[13]</sup>

Recent advances in heart valve modeling have incorporated parametric approaches to successfully describe the valve geometry. Xu *et al.*<sup>[14]</sup> utilized the design properties offered by parametric modeling to develop a design process for a patient-specific bioprosthetic aortic heart valve based on several key geometric valve parameters. They began with a patient-specific aortic root and created surfaces for the leaflets from the NURBS defined by *three design variables*. They varied these parameters to alter the valve design using the Rhinoceros 3D and Grasshopper software (Robert McNeel & Associates) in which the model was created.<sup>[14]</sup> Kamensky *et al.*<sup>[15]</sup> constructed a NURBS TV model using dimensions from Stevanella *et al.* combined with segmented  $\mu$ CT image data from an *ex vivo* ovine heart for the chordae and annulus. They also simulated the rupture of one chorda tendinea, resulting in leaflet prolapse and thus valve regurgitation. As a result, this

was the first TV model that used isogeometric analysis (IGA) and the first to consider a pathological modification; however, this valve was not fully parameterized.<sup>[3]</sup> Lee *et al.*<sup>[3]</sup> expanded the Kamensky *et al.* model by fully parameterizing the TV and adding more valve and chordae configurations to allow for modeling of healthy, diseased, and patient-specific TVs. This model used scanned  $\mu$ CT images to create a B-spline fit of the annulus, then defined the commissure and leaflet heights. The free edge of the leaflets was determined from these heights, and the chordae were then attached to the free edge, completing the geometry model. The present work incorporates a version of this model with a simplified chordae structure. Utilizing the many advantages of IGA for optimization,<sup>[16]</sup> this study aims to maximize the TV performance based on the coaptation area, which Xu *et al.*<sup>[14]</sup> described as the key metric for evaluating heart valve performance, since it reduces the possibility of regurgitation.

## 2.3 Tricuspid Regurgitation

TR occurs when the TV leaflets do not properly close during systole, allowing blood to flow backwards from the right ventricle into the right atrium. TR is classified as either primary or secondary. Primary regurgitation is caused by deformity in the structure of the TV itself, such as from Ebstein's anomaly (i.e., a congenital disease) or from rupture of some chordae, causing one of the leaflets to fail (see Fig. 2.9 for a depiction of Ebstein's anomaly). Secondary TR, also known as functional TR, is when the TV is intact but alteration to the surrounding heart geometry causes improper closure. Examples of functional TR include dilation of the TV annulus, pulmonary hypertension, or enlargement of the right ventricle.

Functional TR will usually progress from three connected pathologies that begin with a pressure or volume overload within the right ventricle. The overload causes enlargement of the right ventricle. Come *et al.*<sup>[17]</sup> found pa-

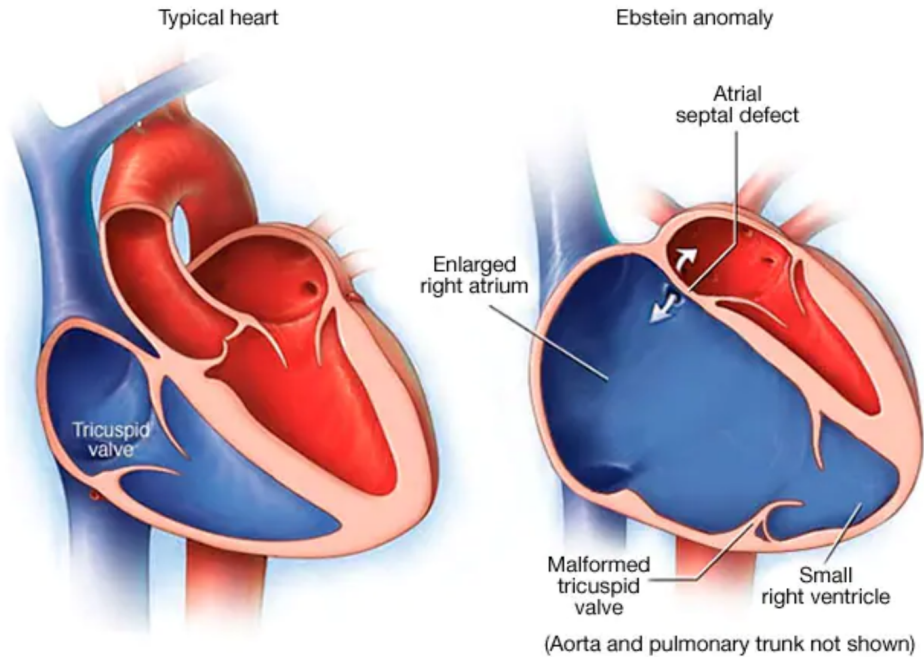


**FIG. 2.9** A depiction of Ebstein's anomaly. Image adapted from mayoclinic.org

tients with TR to have a 60% increase in the diameter of the right ventricle compared to healthy patients. The valve annulus will also deform, dilating away from the septum to enlarge to a more circular shape as compared to the elliptical shape of a healthy annulus. The annulus also flattens, losing its saddle-like configuration. Figure 2.10 depicts these deformations found in functional TR. These three alterations worsen as functional TR progresses, additionally leading to displacement in papillary muscles, leaflet tethering, and reduced leaflet coaptation.

TR affects approximately 1.6 million Americans<sup>[19]</sup> but was historically ignored in the clinical setting due to an initial assumption that right-sided heart lesions would regress naturally with treatment of left-sided lesions.<sup>[20]</sup> Dreyfus *et al.* showed this assumption to be invalid in their 2005 study, leading to an increase in attention in both clinical and research settings, but existing research is still far behind that of the mitral and aortic valves; Fig. 2.11 depicts the number of citations and publications involving research of each

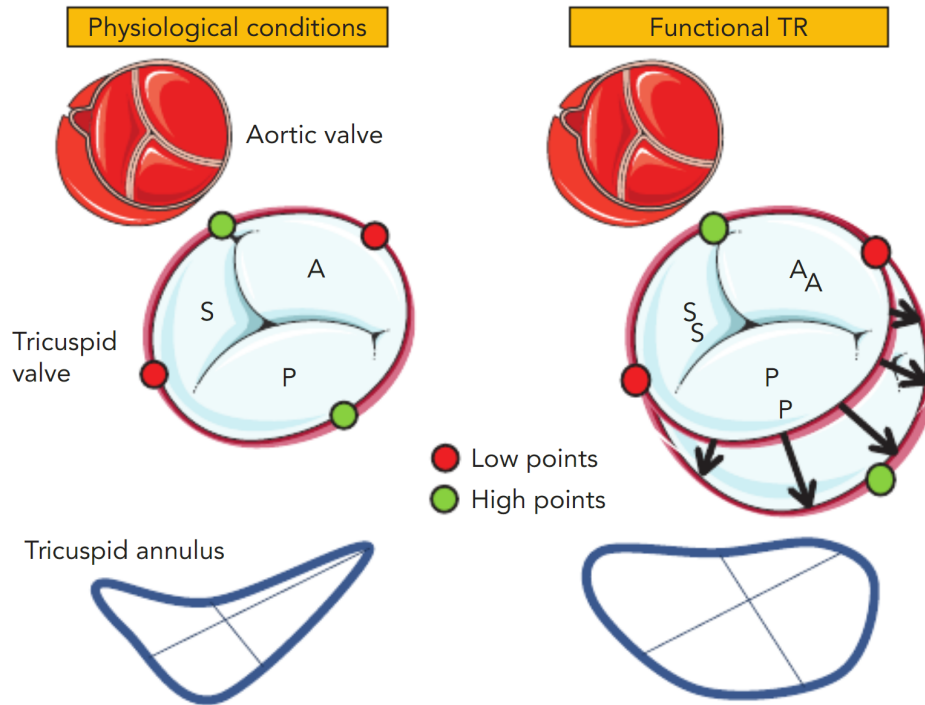


**FIG. 2.10** A healthy tricuspid annulus (left) and a flattened and dilated tricuspid annulus exhibiting functional TR (right). Image adapted from Besler *et al.*<sup>[18]</sup>

heart valve, with research for the TV lagging far behind the other three valves.

Clinicians rely on a variety of medical imaging modalities to diagnose TR, including echocardiography, magnetic resonance imaging (MRI) and CT. Two-dimensional transthoracic echocardiography (2DTTE) is the most commonly used method for assessing the TV, and pairing with color flow imaging such as color flow Doppler can allow for visualization of the regurgitant flow, such as in Fig. 2.12.

Functional TR can be treated by fixing the annulus in a contracted position to restore full closure of the valve leaflets. One method for this, introduced in 1971 by Carpentier, is suturing a soft-plastic annuloplasty ring to the TV annulus, as depicted in Fig. 2.13. Another option introduced in 1973 by Vega *et al.*<sup>[22]</sup> is a suture annuloplasty, surgically placing a continuous suture on the annulus to constrict it. These methods both suffer from a

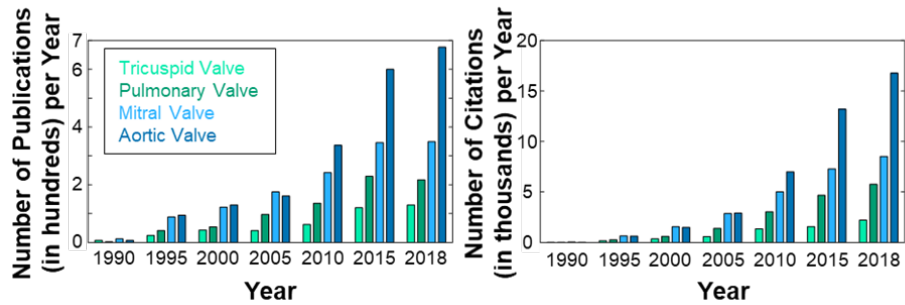


FIG. 2.11 Publications (left) and citations (right) related to the four heart valves since 1990. Image adapted from Lee *et al.*<sup>[3]</sup>

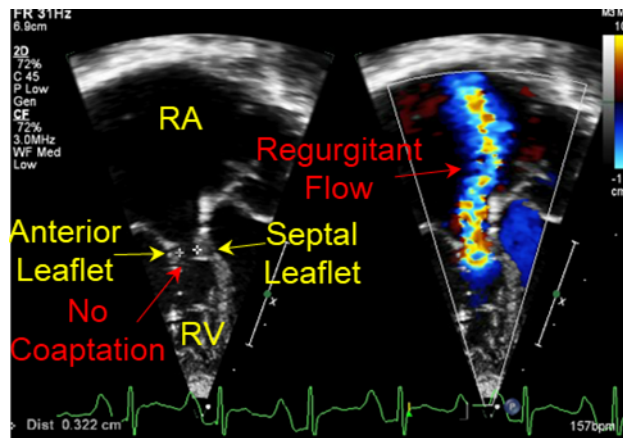
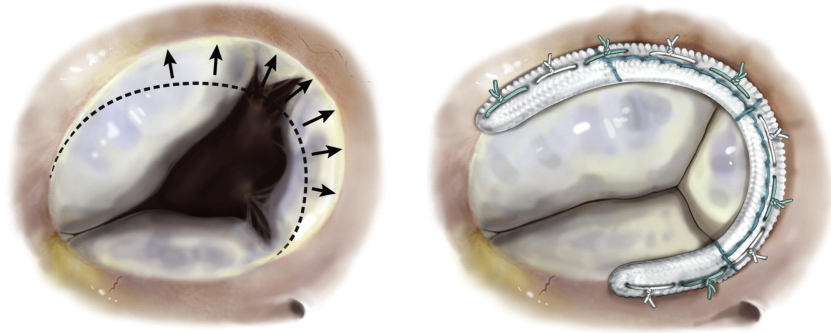


FIG. 2.12 2DTTE (left) and color Doppler imaging (right) of the four-chamber view of an infant patient with pulmonary atresia. Image courtesy of Children's Heart Center at the OU Health Sciences Center.

TR recurrence rate of around 20% within 5–10 years of surgery, though, suggesting that annuloplasty does not address all issues present with functional TR. When regurgitation is caused by rupture of the chordae tendineae leading to leaflet flail or prolapse into the atrium, other treatment options are considered. These include replacing the damaged chordae with fabricated chordae, shortening the chordae to prevent prolapse, and moving chordae from leaflets that are not prolapsing to those that are. These methods have found success in the mitral valve, but shortcomings include mismatch between the mechanical properties of the new and native chordae and rupture of the native chordae tendineae.



**FIG. 2.13** Tricuspid annulus dilation (left) and repair using a soft-plastic annuloplasty ring (right), adapted from Milla *et al.*<sup>[23]</sup>



## 3 GEOMETRY MODELING PIPELINE

3.1 Digitizing Heart Valve Surfaces . . . . .	20
3.2 Rhinoceros and Grasshopper . . . . .	22

Other research has used computational models to improve the understanding of the TV function. In the first example of this, the 2010 work by Stevanella *et al.*<sup>[2]</sup>, they took physical measurements of heart valve dimensions to create their model. The first attempt at generating a patient-specific TV model, however, was not until the 2018 work by Kong *et al.*<sup>[11]</sup> They segmented computed tomography scans of three healthy patients' tricuspid valves and smoothed the results, then meshed the surface for finite element analysis to simulate valve closure. The most recent work by Singh-Gryzbon *et al.*<sup>[12]</sup> in 2019 used a similar approach with a micro-CT scan of an excised porcine heart that was segmented, smoothed, and meshed, but also integrated fluid-structure interaction. They also took steps towards simulating a diseased scenario by displacing the papillary muscle tips of the excised valve at distances found in Spinner *et al.* (2011)<sup>[24]</sup> to mimic conditions present with regurgitation. These previous studies have laid a foundation for patient-specific modeling of the tricuspid valve but lack an adaptability necessary for modeling a wide variety of scenarios necessary for broader clinical application.

This chapter describes in detail each step in the geometry modeling pipeline. The pipeline consists of two major components. In the first part of the process, heart valve surfaces are digitized into point clouds that are used to create the base geometry for the model (Section 3.1). In the latter component, input parameters are combined with the base geometry generated during the digitization stage to form a model in the CAD software Rhinoceros 3D. This model is generated and manipulated in Rhino through the visual programming plugin Grasshopper 3D. As described in this chapter, this manipulation can be used to generate a wide variety of TV models, with an example given.

### 3.1 Digitizing Heart Valve Surfaces

Obtaining *in vivo* scans of the heart with sufficient resolution for accurate characterization of heart valve structures, especially leaflet thicknesses and chordae tendineae, is not possible with current clinical imaging modalities. Instead, we use  $\mu$ CT images of excised tricuspid and mitral valves to create the base for our model, obtained from four fixed porcine hearts. We further subdivide the digitizing process into two steps: (i) placing points along the top surface of the valve within the 2D  $\mu$ CT space, and (ii) combining and transforming those individual 2D data sets into the 3D space.

Four tricuspid and four mitral porcine valves were fixed and scanned in two directions with a high-resolution  $\mu$ CT scanner. Defining the  $z$ -direction as roughly perpendicular to the plane of the closed valve,  $x$ - $z$  scans were taken every 0.118 mm in the  $y$ -direction and  $y$ - $z$  scans were taken every 0.118 mm in the  $x$ -direction. The scans were then digitized manually using an open-source MATLAB program called GrabIt (displayed in Fig. 3.1) using the following procedure.

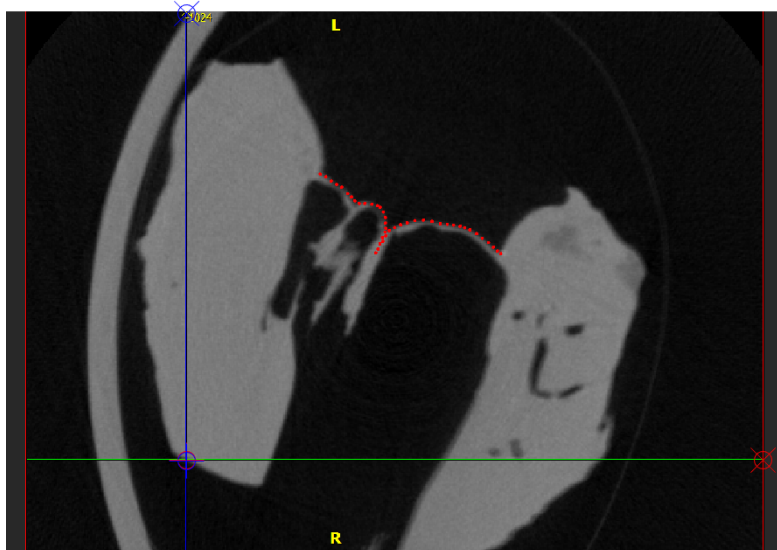


**FIG. 3.1** TV surface mapped in GrabIt. The  $x$  and  $y$  axes are normalized from 0 to 1.

1. A selection of  $\mu$ CT “slices,” 2D images in the  $x$ - $z$  or  $y$ - $z$  plane, are imported into the program, one from every five images so that each slice to be mapped is 0.59 mm from the others.
2. The two axes in each scan are normalized to create a parameter space spanning zero to one.
3. The leaflet surfaces are identified in the scans, and points are placed along these surfaces from the valve annulus on one side to the annulus on the opposite side, creating a continuous line of points along the top surface of the valve.
4. A Microsoft Excel sheet is used to track which points correspond to which leaflet surface (anterior, posterior, or septal leaflet).
5. When multiple leaflets are present in a scan, as is the case for most slices, the contact area between the leaflets is also mapped where possible by placing points along the line where the leaflets make contact.

After the leaflet surfaces are mapped manually, the data is transformed using an in-house MATLAB script. This script converts points from the nor-

malized local coordinates to their absolute coordinates and then combines points for all slices into a single point cloud data vector. It also identifies the points in the point cloud corresponding to the valve annulus, which are the outermost two points of each slice. The script then exports these data as two separate text files, one containing the Cartesian coordinates of all points and the leaflet they correspond to, and the other containing the coordinates of the annulus points. Since scans were performed along both the x- and z-directions, each valve has two corresponding sets of  $\mu$ CT slices and two point clouds. An example point cloud is shown in Fig. 3.2.

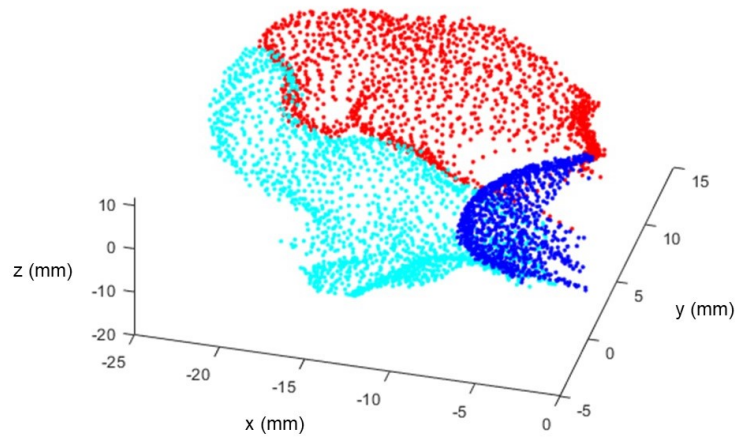


**FIG. 3.2** TV point cloud generated in MATLAB using absolute coordinates for all points.

## 3.2 Rhinoceros and Grasshopper

The TV is modeled in the program Rhinoceros 3D (Rhino), a CAD software using NURBS to represent geometry. The advantage of using NURBS for modeling is that the geometry can then be directly used for analysis without an intermediate meshing step in a process known as IGA. This analysis using IGA is described in further detail in Chapter 5. Though the actual model

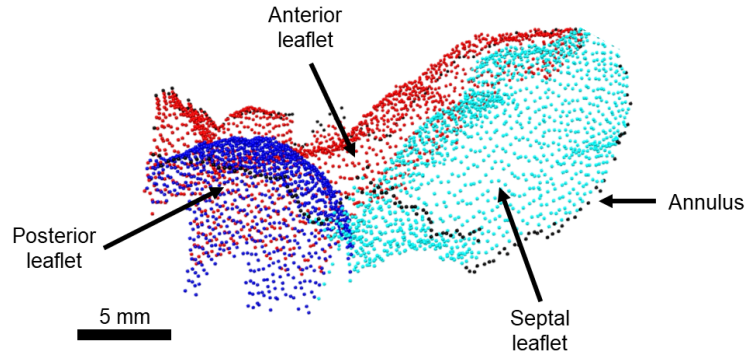


**FIG. 3.3** TV point cloud, with annulus points in black, anterior leaflet in red, posterior leaflet in cyan, and septal leaflet in blue.

is located within Rhino, it is built using a program called Grasshopper 3D, a visual programming language plugin for Rhino. The plugin uses components dragged onto a canvas to perform different operations both within and outside of Rhino. These components are connected to one another using wires which pass data between the components. Using Grasshopper to create the model is essential to the parametric approach used for the model since it is able to automate updates to the model instantaneously as parameters are provided.

Input data for the model is read from the text files containing the point cloud and annulus point cloud for a TV, which is saved in a particular location. Figure 3.3 depicts an example TV point cloud in Rhino. First, the annulus is constructed. The annulus points are sorted around the plane of the annulus, then interpolated into a cubic curve, shown in Fig. 3.4. This initial curve does not provide a good fit for the annulus, as it is interpolated through each of the annulus points. It does provide a good baseline, however, to use in identifying the beginning annulus point for each leaflet. The curve is then rebuilt using a specified number of control points to smooth it, giving it a more accurate annulus representation (Fig. 3.5). The new, rebuilt curve is a cubic periodic B-spline curve with control points defined using three-dimensional cylindrical coordinates. Three of the control points

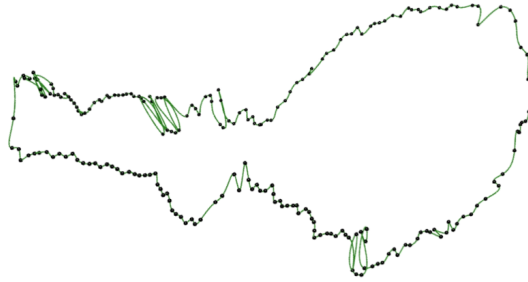


**FIG. 3.4** Annulus points with curve interpolation.

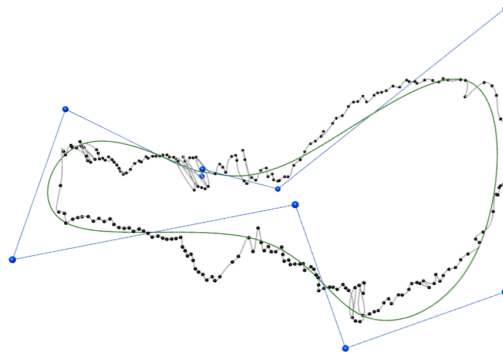


**FIG. 3.5** Rebuilt annulus NURBS curve with control polygon in blue

overlap to ensure smoothness between the beginning and end of the curve. The plane of the annulus is defined using a least squares fitting algorithm to fit a plane to the constructed annulus curve.

After the annulus is constructed, the surface for the leaflets is created. The three commissures are identified within the annulus points using the boundaries between leaflets, since each annulus point drawn from the input point cloud is identified with a certain leaflet. Six points are defined around the annulus along the one-dimensional parametric space of the annulus curve, corresponding to the three commissures and center points of the three leaflets (Fig. 3.7). These points are used to parametrize the leaflets, shown in Fig. 3.6, using six dimensions. Distances for each of the six annulus points are used to offset points from the annulus in a direction perpendicular to the best-fit plane of the annulus. These distances become the “height” of the leaflet surface at these points. The heights are read from

a text file containing the parameter values, which is defined outside the Grasshopper environment so it can be altered by other programs involved in the model. Six lines are generated between the annulus and offset points, which are then reformulated as straight cubic NURBS curves (Fig. 3.8). These are the lines that will be used to generate the open leaflet surface.

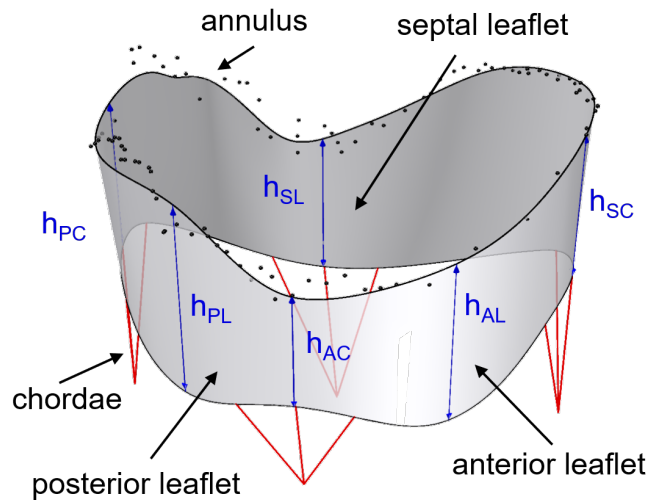


**FIG. 3.6** The six parameter heights used for the tricuspid valve model: anterior, posterior, and septal leaflets ( $h_{AL}$ ,  $h_{PL}$ , and  $h_{SL}$ , respectively), and postero-septal, antero-septal, and anteroposterior commissures ( $h_{PC}$ ,  $h_{SC}$ , and  $h_{AC}$ , respectively).

The free edge of the leaflet is created by interpolating a third-degree NURBS curve around the six offset points, shown in Fig. 3.9. This, along with the annulus curve, is then used to generate a Gordon surface, which is a thin

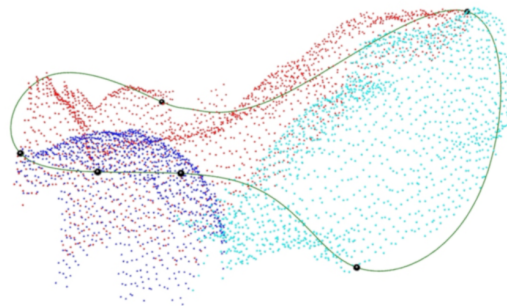


**FIG. 3.7** Leaflet and commissure locations along the annulus curve.

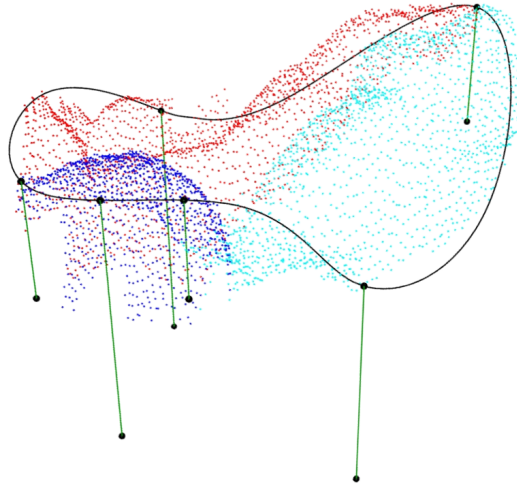


**FIG. 3.8** Leaflet and commissure heights offset from the annulus.

surface passing through a series of curves which define it. In this case, the surface passes through the six curves created from the offset points, which represent the leaflet and commissure heights. When generated in this manner, the NURBS surface has over 100 control points in the  $u$ -parametric direction (around the surface in the same direction as the annulus) and only six in the  $v$ -parametric direction (along the path from the annulus to the free edge), as in Fig. 3.10a. The surface is regenerated to use one-third the number of points in the  $u$ -direction and two additional points in the  $v$ -direction to create a more evenly-distributed mesh of control points (Fig. 3.10b). The leaflet surface with its constructing curves is shown in Fig. 3.11.

Once the leaflet surface is constructed, the chordae tendineae are defined. Though  $\mu$ CT scans have a high resolution, *in vivo* imaging modalities are typically unable to capture the full chordae configuration. For this reason, chordae definition in this model is a much more open, flexible process compared to the leaflet surface definition. Papillary muscles in the ventricle are typically found in three groups, though the posteroseptal and sometimes anteroseptal groups often have two muscles in a group.<sup>[2,25]</sup> To account for this, we define four points representing papillary muscle attachment points in the model which connect to the chordae tendineae. Each



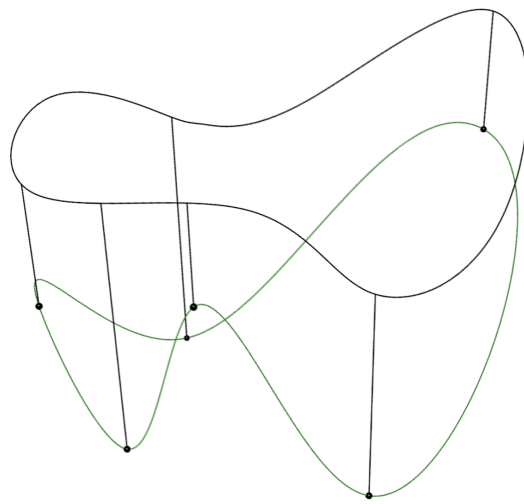


**FIG. 3.9** Interpolated leaflet free edge.

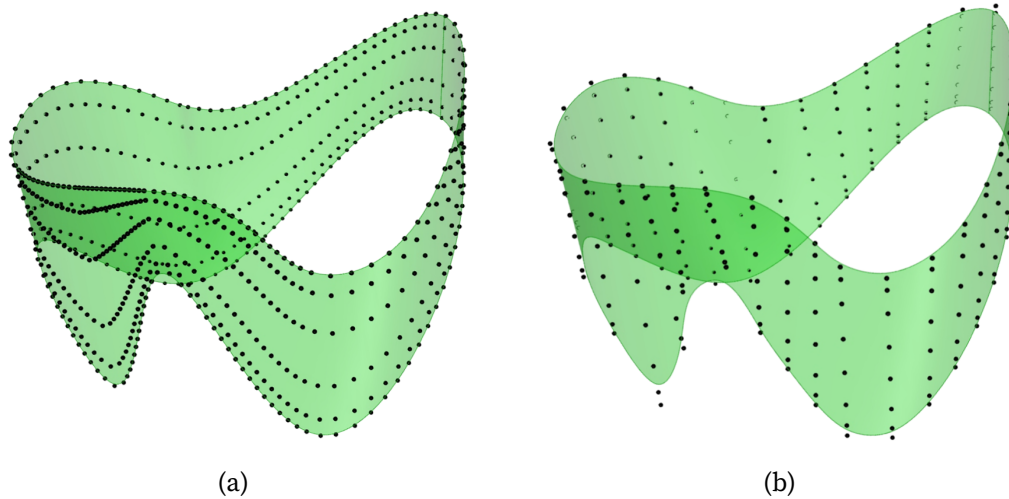


**FIG. 3.10** (a) Leaflet surface with initially generated control points and (b) rebuilt leaflet surface with more evenly distributed control points.

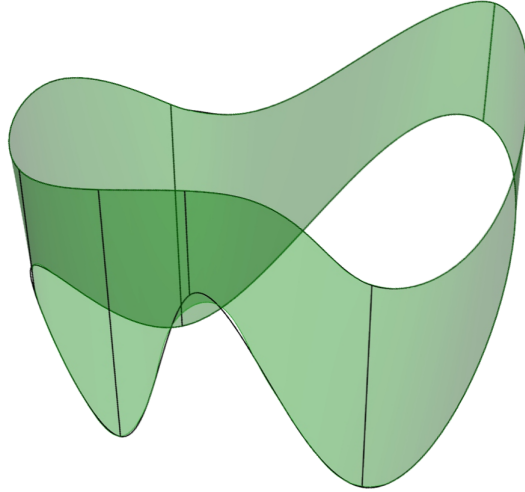


**FIG. 3.11** Gordon surface created using the annulus and free edge curves and six leaflet height curves.

point is defined by a vertical distance from the annulus, an offset distance perpendicular to the annulus, and a location in the  $u$ -parametric direction around the annulus. Determining where to locate these points can be a challenging problem. Singh-Gryzbon *et al.* included the papillary muscles in their segmentation, but had to manually rebuild some chordae due to needing to mesh the papillary muscles and chordae as well as the leaflets. Aversa *et al.*<sup>[10]</sup> had difficulty identifying papillary muscles in their volumetric DICOM data, so used the sonomicrometric data reported by Hiro *et al.*<sup>[5]</sup> In this work, we can overlay the  $\mu$ CT volumetric scan data over the valve model, matching the scan annulus with the model annulus, and manually place papillary muscle points, as shown in Fig. 3.12. Note that in this example, the anteroseptal papillary muscle was not obtained in the scan and its position had to be approximated based on the chordae direction.

The chordae attach from the point defined as the papillary muscle attachment to a corresponding location on the leaflet. Stevanella *et al.* found chordae to attach either at the free edge or at approximately two-thirds of the leaflets' height. We usually attach the chordae in the model at the free edge, but we can vary this attachment location to anywhere along the  $v$ -

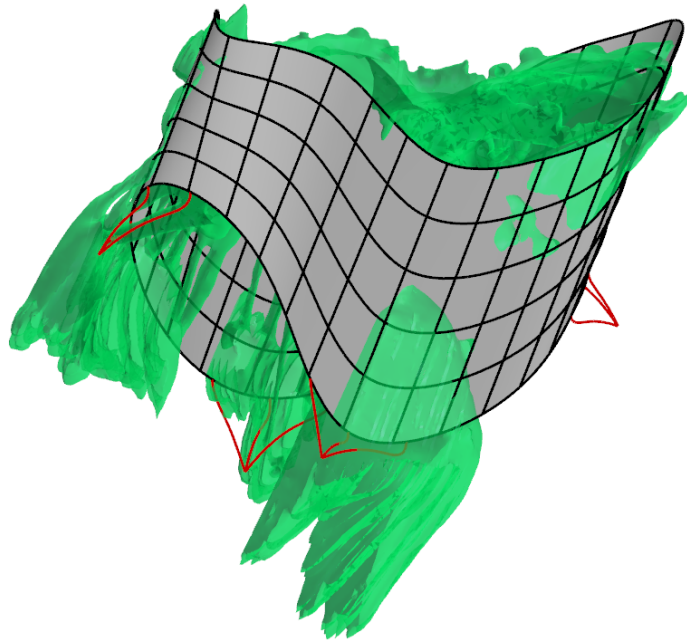


**FIG. 3.12** TV model superimposed with  $\mu$ CT scan data including papillary muscles (green).

parametric direction. The number of chordae in each chordae grouping and the spacing between each chord can additionally be varied. To prevent the chordae from interfering with the leaflet surface during valve closure, a tangency condition is enforced between the chordal attachment to the leaflet and the leaflet surface.

If the free edge of the TV leaflet is defined according to the annulus and height parameters and the papillary muscle locations are fixed, this does not leave room for variance in pre-stretch length if simple beam elements are used for the chordae, depicted in Fig. 3.13. While this is unimportant if both the papillary muscle locations and chordae lengths are known, these two quantities can be difficult to identify. The chordae from excised valves can be measured, as in Stevanella *et al.*<sup>[2]</sup>, but papillary muscle locations will need to be approximated. *In vivo* imaging can identify papillary muscle positions relative to the annulus, but individual chordae can be difficult to capture, as seen in Singh-Gryzbon *et al.*<sup>[12]</sup>

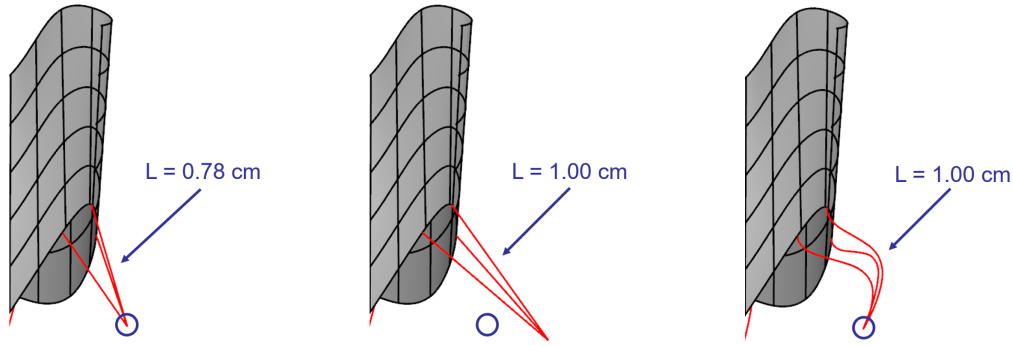


**FIG. 3.13** A straight chordae model forces dependence between chordae length and papillary muscle locations. In this example, the desired papillary muscle attachment is shown in the blue circle and the desired chordae length is 1.0 cm. The curved chordae on the right do not have this limitation.

For this reason, we define a third point for each chorda between the papillary muscle attachment and leaflet attachment. This point is offset from the straight line between the two points, and a B-spline curve is interpolated through these three points to form the chordae tendineae. By varying this offset distance in the input parameter file, we can adjust the initial unstretched length of the chordae. This gives the model more flexibility, enabling testing of valve closure with different contracted papillary muscle conditions without varying chordal lengths or vice versa such as in the case of model optimization, explored in Section 5.2. Simple beam chordae can still be tested by simply setting the offset parameter to zero. The model with the constructed chordae additions is depicted in Fig. 3.14.

The final TV model is shown in Fig. 3.15, and represents the final stage in the modeling pipeline. Fig. 3.16 gives an overview of the modeling pipeline. The data inputs for the model are the  $\mu$ CT image data and the input parameter file.  $\mu$ CT image data is obtained from fixed porcine valves and the valve surface is manually mapped aided by GrabIt. The individual slice surfaces are combined and scaled using MATLAB to create a point cloud. Values for the input parameters are obtained from measurements, literature, or exper-

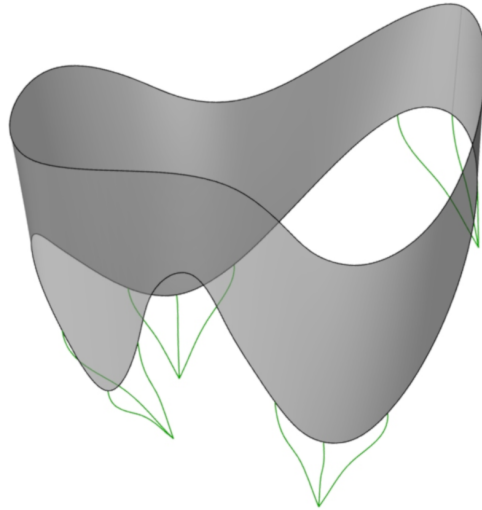


**FIG. 3.14** Four three-strand chordae groups added to the TV leaflet surface model.

imental values in the case of model optimization. The point cloud and input parameter file are then fed into the modeling framework built in Grasshopper, creating the final model in Rhino. This model is immediately able to be analyzed for closure without meshing, as its components have all been constructed from NURBS. This analysis process is explored in Section 5.1.

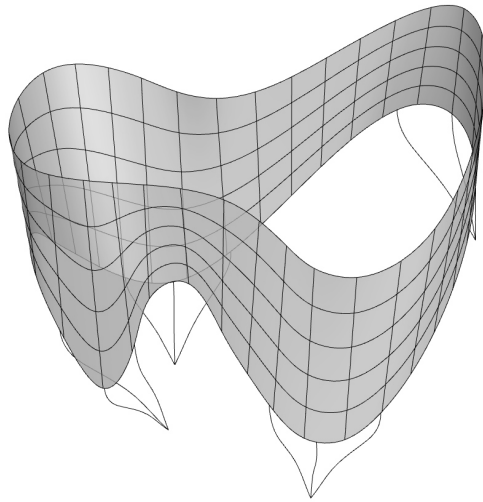


FIG. 3.15 Completed TV model.

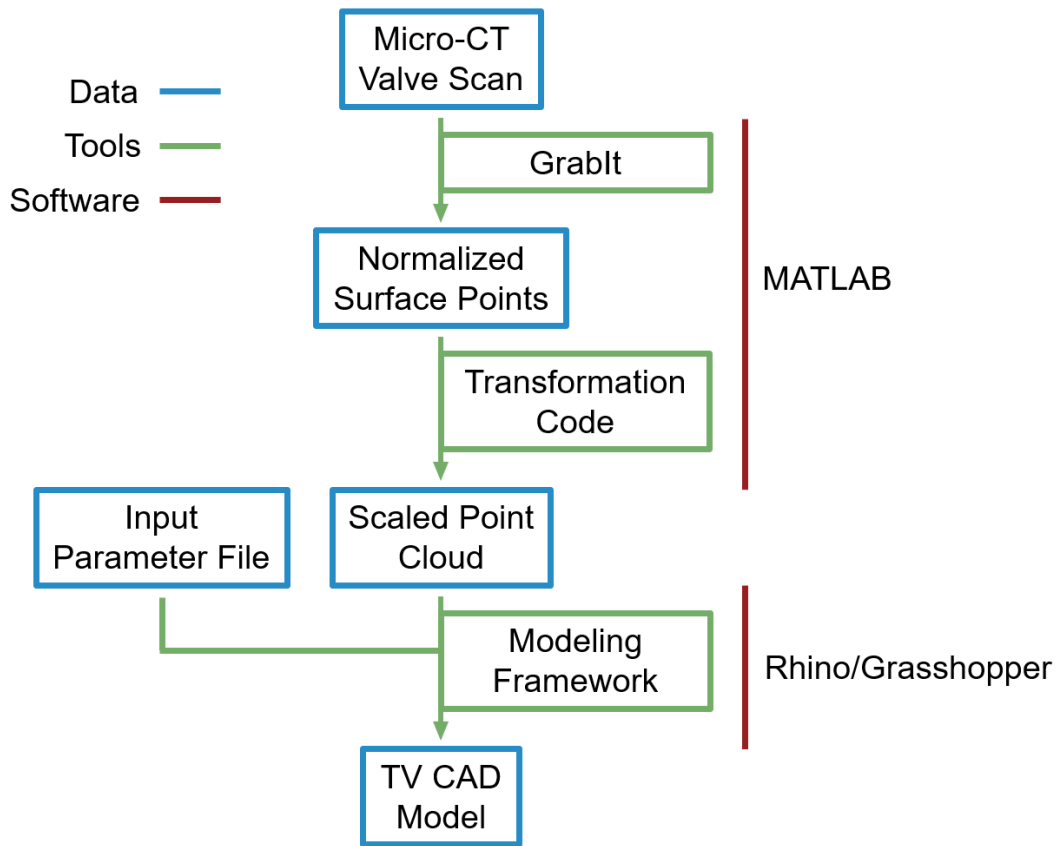


FIG. 3.16 Overview of the developed TV model pipeline

## 4 GEOMETRY MODELING EXAMPLES

4.1 Tricuspid Valve Geometries . . . . .	33
4.2 Adaptability of the TV Model . . . . .	41
4.3 Application to the study of the Mitral Valve . . . . .	43

### 4.1 Tricuspid Valve Geometries

We carry out the process outlined in Chapter 3 for four different TV data sets to demonstrate the capabilities of the proposed pipeline. For all four data sets, we use a set of input heights for the commissures and leaflets that falls within the range reported by Stevanella *et al.*<sup>[2]</sup> The heights chosen for this demonstration are shown in Table 4.1.

Figure 4.1 summarizes the process for the model fitting to the first set of  $\mu$ CT data, TV-1. Figure 4.1a gives the input data set after the surface has been mapped and digitized into point cloud. Note the saddle-like shape of the annulus in the input point cloud that is reflected in the final model. Also note the locations of the commissures and centers of each leaflet, marked in Fig. 4.1b. For these data, the annulus lengths for each leaflet are similar, leading to a relatively even distribution of height parameters. The septal

**TABLE 4.1** Leaflet and commissure heights used for the four TV models.

	Height (mm)
Anterior leaflet	12.88
Posterior leaflet	15.18
Septal leaflet	15.75
Anteroposterior commissure	4.63
Posteroseptal commissure	6.16
Anteroseptal commissure	6.18

leaflet is typically the largest of the three, and this is reflected here in both the input point cloud and the final model.

Figure 4.2 shows the model fit for TV-2, which is the data that was used as an example in Chapter 3. Again, the annulus has a distinct saddle shape, very similar to the TV-1 data. For this valve, the commissures and leaflet centers, marked by the black points in Fig. 4.2b, are not as evenly spaced. The annulus length for the posterior leaflet is much smaller than for the anterior and septal leaflets for this set of input data. This causes the heights to be much closer to one another for this part of the model. The result is a more extreme curvature along the free edge between the posterior leaflet and the anteroposterior commissure and a relatively small posterior leaflet in the final model, as seen in the original data.

The third set of TV scan data varies from the other data sets. Figure 4.3 shows a close-up of the TV in the heart sample itself alongside a three-dimensional view of the  $\mu$ CT image data for TV-3. To better identify the leaflets in the scan, Figure 4.4 shows the highlighted leaflets. This valve has a much more prominent septal leaflet which dominates the center of the valve, even appearing to make contact with the annulus on the other side, contrasting the other data which have more even distributions between the three leaflets.



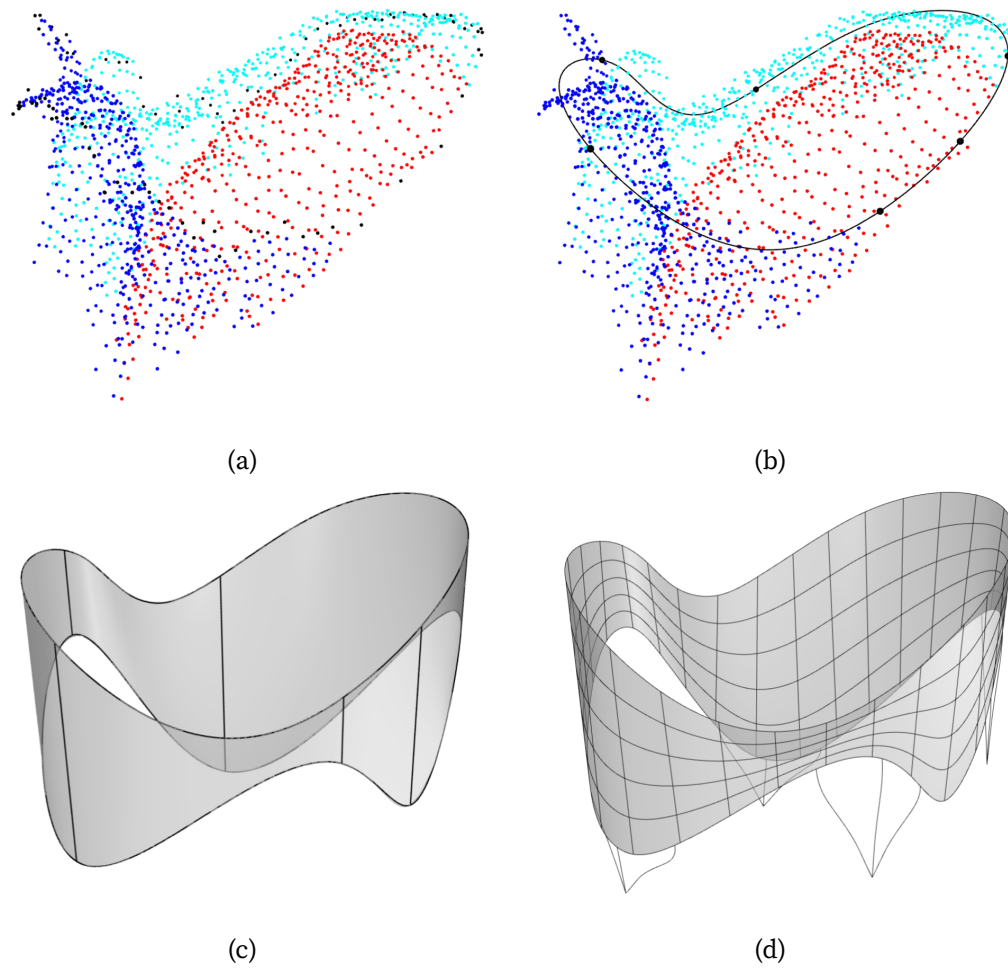


**FIG. 4.1** TV-1 leaflet surface fitting, showing (a) the transformed point cloud, with septal leaflet points in cyan, anterior in red, and posterior in blue, (b) the annulus curve fit with the locations of commissures and leaflet centers, (c) the leaflet surface with leaflet and commissure heights, and (d) the final TV-1 model.

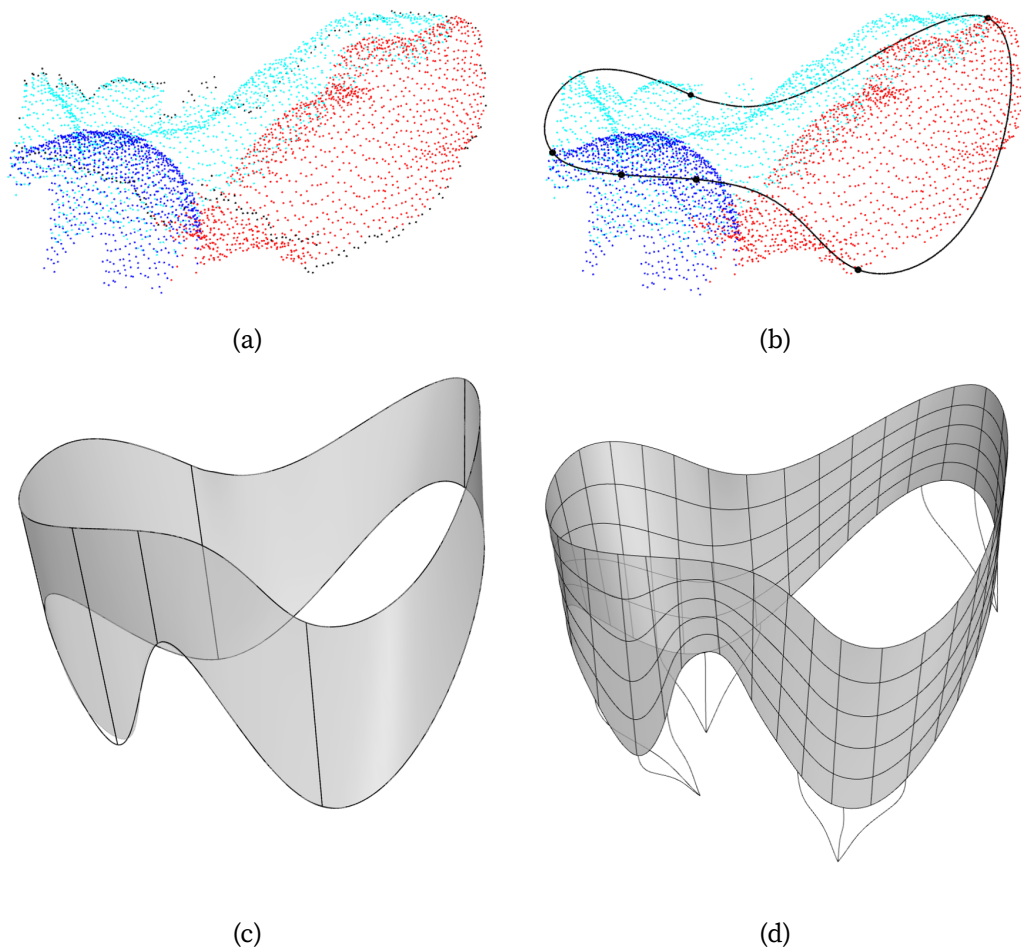
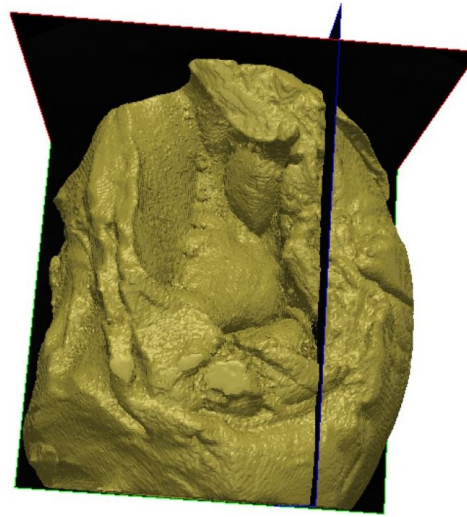


**FIG. 4.2** TV-2 leaflet surface fitting, showing (a) the transformed point cloud, with septal leaflet points in cyan, anterior in red, and posterior in blue, (b) the annulus curve fit with the locations of commissures and leaflet centers, (c) the leaflet surface with leaflet and commissure heights, and (d) the final TV-2 model.



(a)



(b)

**FIG. 4.3** (a) The tricuspid valve in heart sample 3 and (b) the 3-D  $\mu$ CT scan of the excised TV-3.

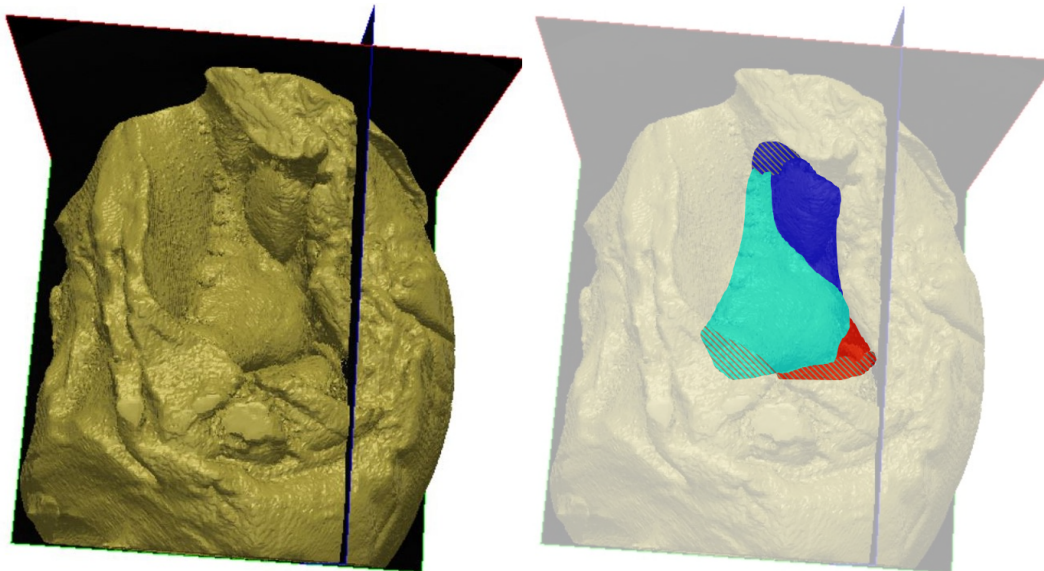


**FIG. 4.4** TV-3  $\mu$ CT scan with the leaflets highlighted: septal in cyan, anterior in red, and posterior in blue. Hatched areas are behind other heart tissue.

To improve clarity of both the point cloud and the valve, Figs. 4.5–4.7 have two viewing angles. As seen in Fig. 4.5, the point cloud captured from the  $\mu$ CT images accurately reflects the actual valve geometry, despite the odd shape. Figure 4.6 shows the resulting annulus curve fit after rebuilding. The annulus has the typical saddle shape expected for the TV in the vertical direction, though the height difference is less pronounced compared to the other data sets. However, when viewed from above, the shape deviates from the oval shape typically seen, with a corner near the posteroseptal commissure. Figure 4.7 shows how this irregular annulus shape affects the overall leaflet surface. The black lines show the rebuilt annulus curve, leaflet heights, and interpolated free edge curve that are used to generate the initial leaflet surface. Chapter 3 described how this surface is rebuilt to use a more even distribution of control points. The gray leaflet surface shown in the figure is this rebuilt surface. In most cases, the rebuilt surface matches the initial surface perfectly or almost perfectly. With TV-3, however, the corner near the posteroseptal commissure is too extreme for the rebuilt surface to match it exactly. This leads to the discrepancy observed in the figure. The final model with chordae tendineae is shown in Fig. 4.8.

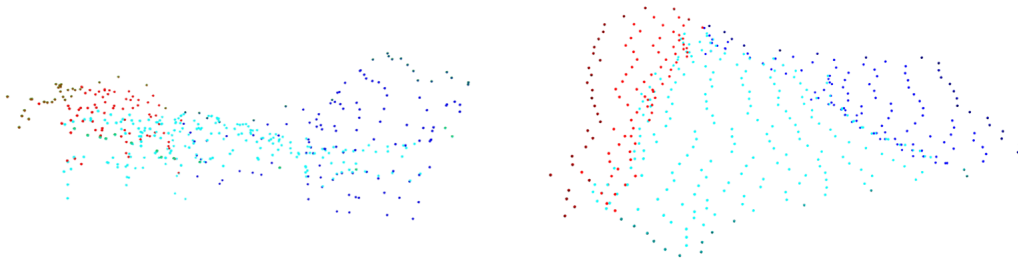


**FIG. 4.5** Transformed surface point cloud for TV-3, side view (left) and top view (right).

It is possible that the odd shape of TV-3 is physiological, but another likely explanation is the way in which it was fixed. Despite the shape, the modeling pipeline is able to accurately digitize the surface and generates a model from the valve annulus. This demonstrates a limitation of the

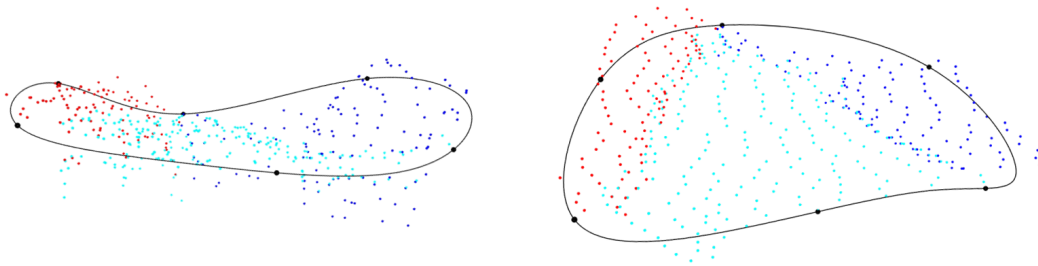


**FIG. 4.6** TV-3 rebuilt annulus curve fit with locations of the leaflet centers and commissures, side view (left) and top view (right).

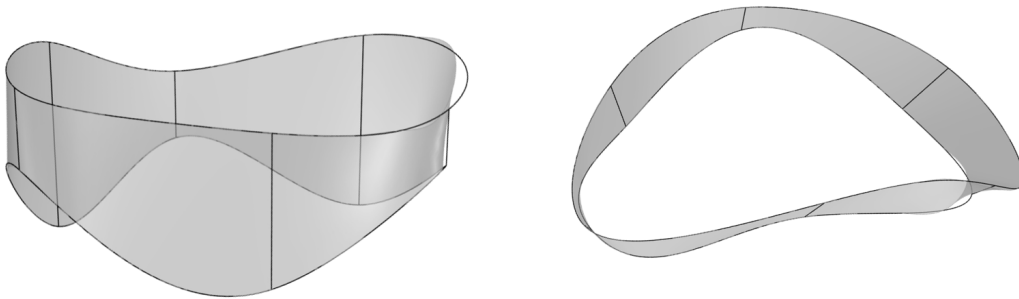


**FIG. 4.7** TV-3 valve surface fit with leaflet and commissure heights, side view (left) and top view (right).

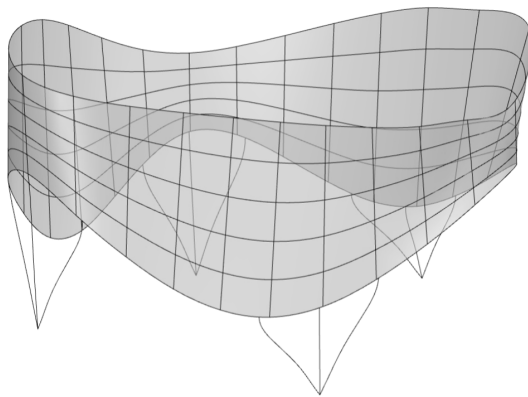


**FIG. 4.8** Final TV-3 model.

pipeline: the quality of the final model is dependent on the quality of the input data at the beginning of the pipeline, as expected.

Figure 4.9 shows a summary of the modeling pipeline for TV-4. The point cloud captures the surface of the valve, though it does not capture very much coaptation of the leaflets. Here, note the hole in the center of the three leaflets. This is not a fault of the digitization process, but again stems from the data input itself. Figure 4.10 displays the fixed and excised TV-4 sample, and the same hole can be seen in the center here. Again, one explanation could be the way the valve was fixed.

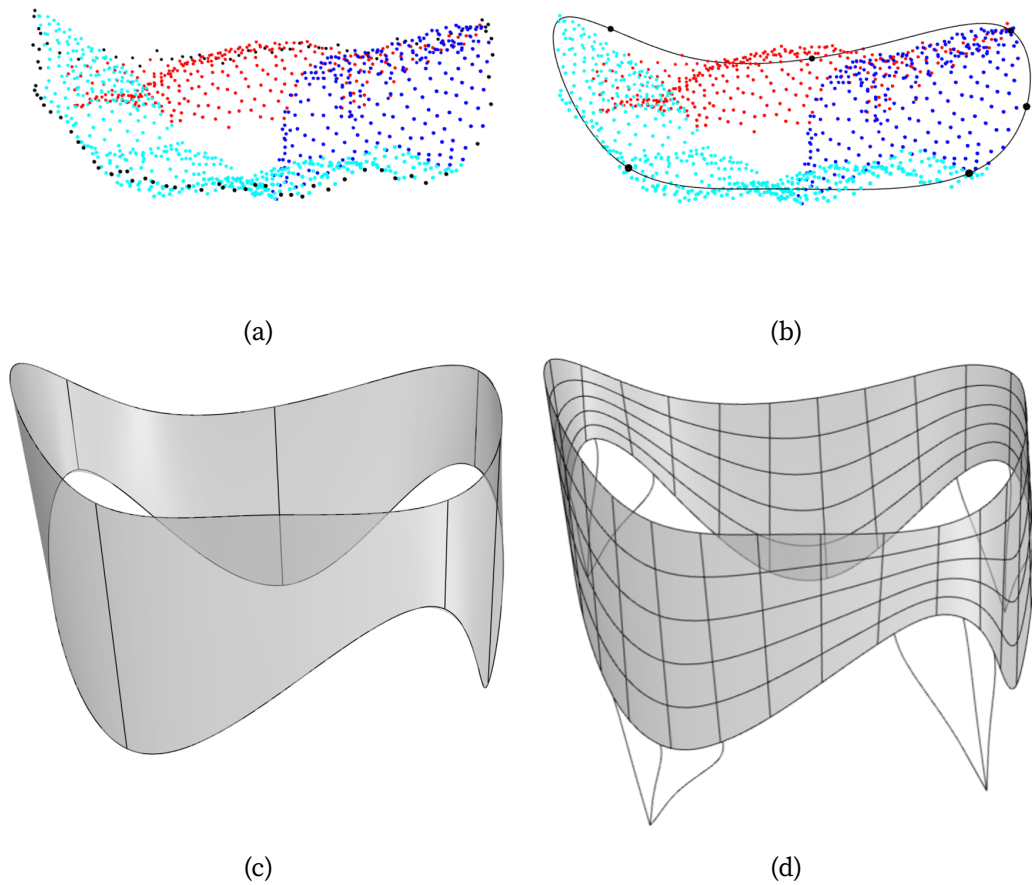


**FIG. 4.9** TV-4 leaflet surface fitting, showing (a) the transformed point cloud, with septal leaflet points in cyan, anterior in red, and posterior in blue, (b) the annulus curve fit with the locations of commissures and leaflet centers, (c) the leaflet surface with leaflet and commissure heights, and (d) the final TV-4 model.

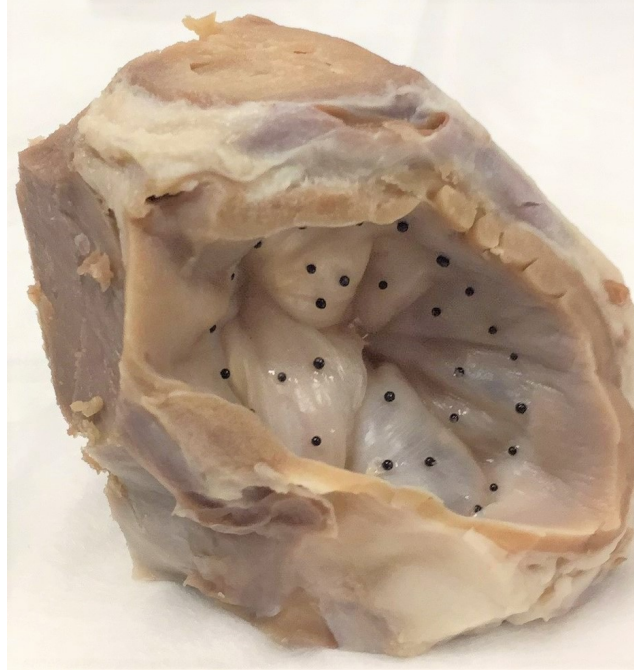
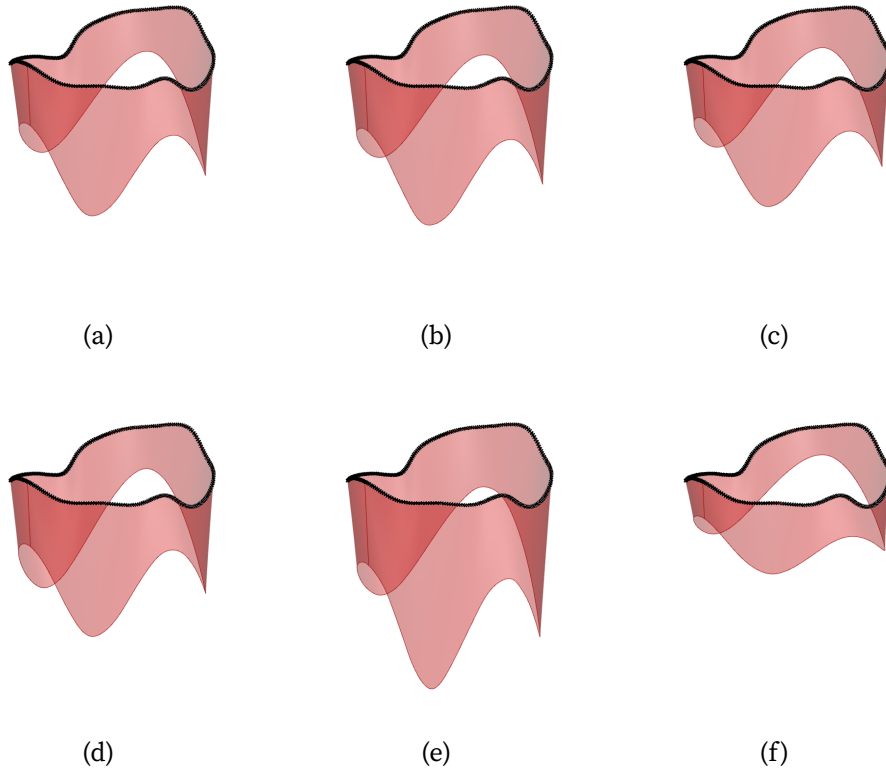


FIG. 4.10 Fixed, excised TV-4 sample.

## 4.2 Adaptability of the TV Model

The creation of the TV model in the Grasshopper programming environment and its reliance on a set of input parameters makes it simple to adjust the model to fit a wide variety of scenarios. As previously demonstrated, the relative heights of the leaflets and commissures can vary significantly. Rather than using published values from literature, we can use different dimension combinations to easily create TV models with shortened leaflets or extended commissures. Combined with the analysis in Section 5.1, we can compare the valve closure of different leaflet sizes. Examples of different leaflet configurations are shown in Fig. 4.11, using values found in Stevanella *et al.*<sup>[2]</sup> as a baseline for feasibility. The same input annulus data is used in these examples, with only the leaflet and commissure heights varying.

Likewise, we can adjust the chordae configurations. The complex branching chordae structure makes it difficult to perfectly model individual



**FIG. 4.11** Different parameter heights for the same annulus data: (a) mean heights from Stevanella *et al.*<sup>[2]</sup>; (b) mean heights plus one standard error and (c) minus one standard error; (d) median heights from Stevanella *et al.*; and (e) maximum and (f) minimum heights measured by Stevanella *et al.*

chordae; however, by adjusting a few parameters in the Grasshopper environment, we can create many simplified chordae configurations to mimic the complex physiological and pathological function. Figure 4.12 shows some examples of different chordae configurations possible with the current modeling pipeline. Many tightly-spaced chordae, such as those seen in Fig. 4.12c and Fig. 4.12f, are more similar to the chordae found in the MV. For the TV, however, the configuration seen in Fig. 4.12a may provide adequate characteristics for accurate modeling. The proposed modeling pipeline, with its ease of use in adjusting such parameters, makes future study into chordae model effectiveness much simpler to undertake.



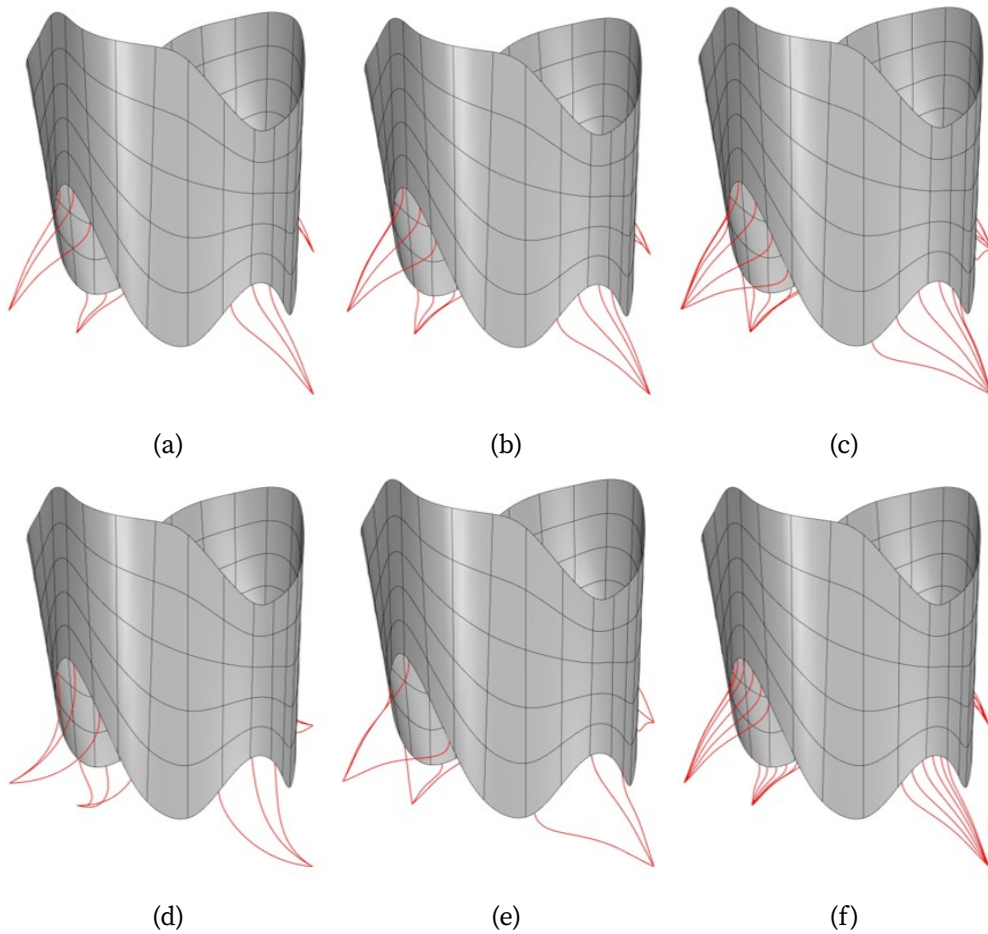


**FIG. 4.12** Different chordae configurations for the same leaflet surface and papillary muscle positions: (a) three, (b) four, and (c) six chordae per group; (d) long chordae; and (e) spaced and (f) close free edge attachments within the group.

### 4.3 Application to the study of the Mitral Valve

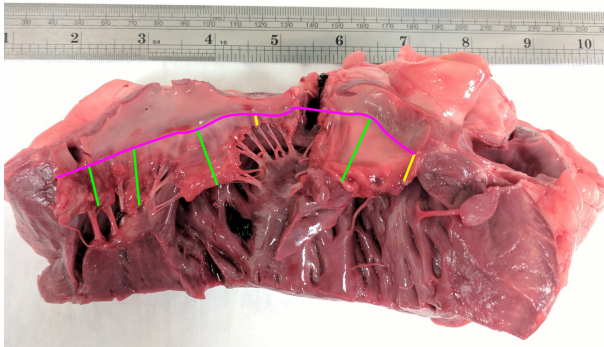
The model can also be generalized to MV data using a similar approach. The MV has only two leaflets, anterior and posterior, and two commissures, anteromedial and posterolateral. Similar to the tricuspid valve, the MV annulus has a saddle shape. The low points in the saddle correspond to the lateral and medial commissures. The anterior and posterior leaflets are each typically subdivided into three sections, numbered 1–3 in the medial to lateral direction. The posterior leaflet takes up a majority of the annular circum-

ference. While the anterior leaflet typically has a relatively smooth, continuous free edge, the posterior leaflet usually has two minor indentations that divide the leaflet into three scallops. The four measurements, consisting of two leaflets and two commissures, would be insufficient to accurately define the geometry of the MV leaflet tissue. Instead, we measure the height of each scallop of the posterior leaflet. When combined with the two commissure heights and the anterior leaflet height, we have six measurements with roughly even spacing, giving a similar level of quality to the MV leaflet geometry when compared to the TV leaflet geometry. Measurements for MVs from six hearts are shown in Table 4.2.

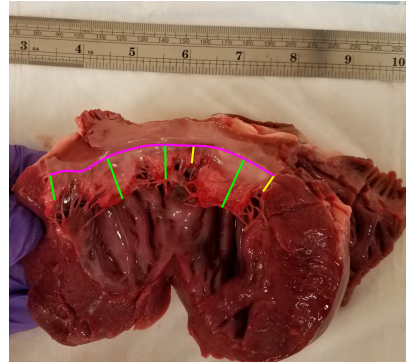
**TABLE 4.2** Leaflet measurements from six MV samples.

MV	Leaflets (mm)				Commissures (mm)	
	P1	P2	P3	A2	Medial	Lateral
1	15.64	21.69	22.44	26.64	4.18	11.00
2	12.71	21.79	16.93	26.64	8.51	9.63
3	12.27	15.60	7.93	21.97	6.40	8.09
4	8.51	15.60	8.40	15.55	3.26	8.13
5	15.44	16.74	11.76	17.24	3.89	6.37
6	11.72	23.71	14.66	20.54	6.87	6.52
Average	12.72	19.19	13.69	21.43	5.52	8.29

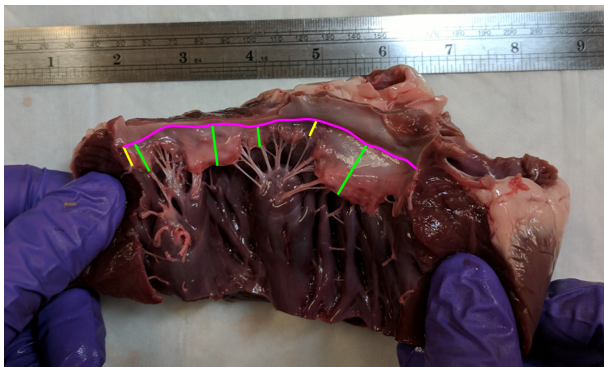
We use the same modeling pipeline developed in Chapter 3 and apply it to the MV. First, we obtain  $\mu$ CT data from four excised porcine MVs. We then manually map the surfaces using GrabIt and combine the surface maps into point clouds using the MATLAB transformation script. Figure 4.14 displays the point clouds for the four MVs. The point clouds are then input into Grasshopper. Figure 4.15 gives an example of the point cloud for MV01 in Rhino after this step.



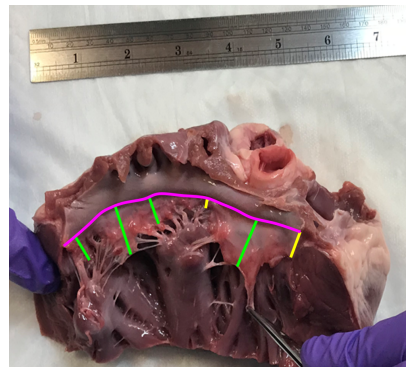
(a)



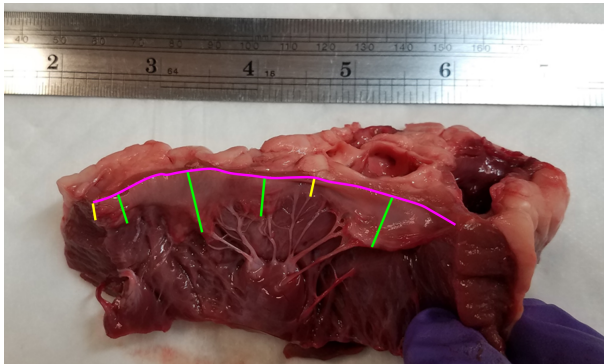
(b)



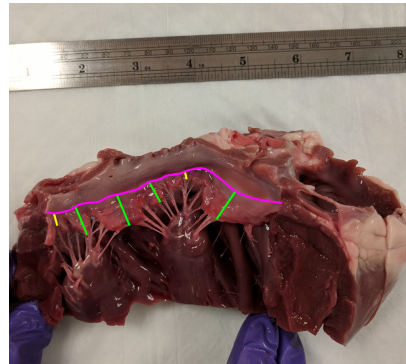
(c)



(d)



(e)



(f)

FIG. 4.13 MV leaflet measurements (green) and commissure measurements (yellow) from six hearts. The annulus is marked in magenta.

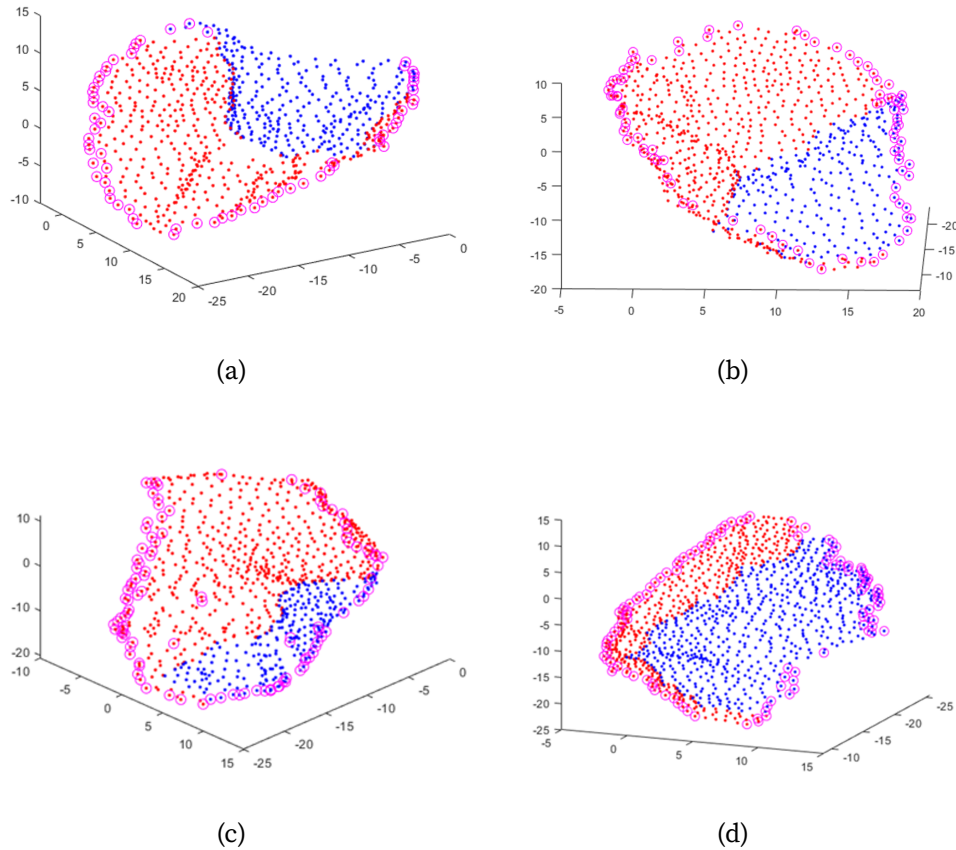


**FIG. 4.14** Point clouds for MVs (a) MV01, (b) MV02, (c) MV03, and (d) MV04. Annulus points are circled in magenta.

The primary change to the pipeline is within the model located in Grasshopper, redefining leaflet and commissure locations, decreasing the quantity of leaflets and leaflet parameters, and adjusting the chordae to reflect the more complex groupings found within the MV. Annulus data is extracted from the point cloud in the same manner. Three height parameters are used for the posterior leaflet, and no septal leaflet is created. For chordae, we use two papillary muscles, and seven chordae strands in each group to better-represent the type of chordae found in the MV. An example model for MV01 is shown in Fig. 4.16. Parameters used for leaflet heights were average values from Table 4.2.

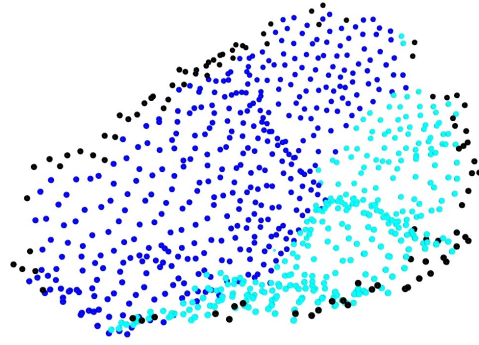


FIG. 4.15 MV01 point cloud in imported into Rhino.

Though there is significantly more research into the MV than the TV, research still lags behind the semilunar valves (see Fig. 2.11 in Chapter 2). The adaptability of the proposed pipeline can be used to bridge the research gap and provide a tool for patient-specific MV research.

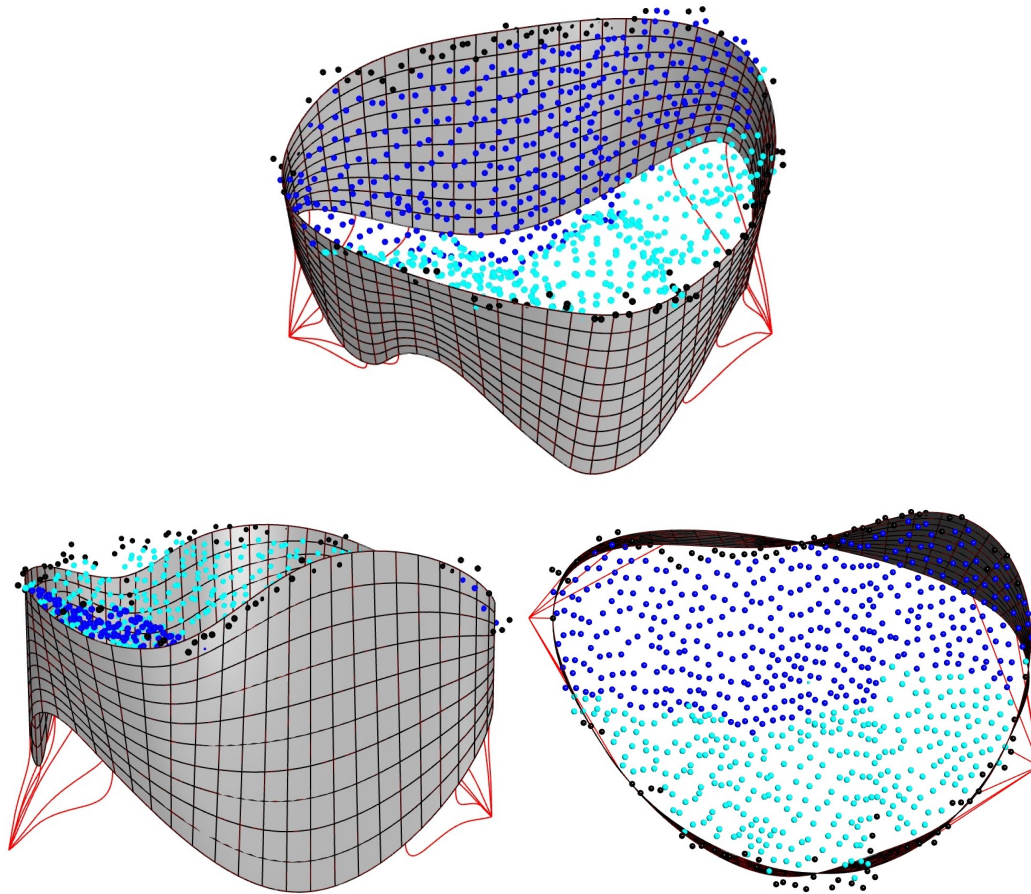


FIG. 4.16 MV01 point cloud and model using average values from Table 4.2.

## 5 MODELING APPLICATIONS

5.1 Isogeometric Analysis . . . . .	49
5.2 Optimization . . . . .	51
5.3 Patient Education . . . . .	55

### 5.1 Isogeometric Analysis

A major advantage of using NURBS for modeling the valve function is that it allows for IGA of the *in silico* simulation by directly performing analysis on the model without an intermediate meshing step, as typically required in performing traditional FE analysis and being most time-consuming. Kamensky *et al.* performed IGA on their TV model in their 2018 paper, and this provides a baseline for IGA on the models generated using the modeling pipeline.

To model the soft tissue of the leaflets, we assume the tissue is incompressible and described by a Lee–Sacks material model (Lee *et al.*) as described in Wu *et al.*<sup>[26,27]</sup> We compute the second Piola–Kirchhoff stress  $\mathbf{S}$  from the Green–Lagrange strain  $\mathbf{E}$  using

$$\mathbf{S} = 2 \frac{\partial \psi_{el}}{\partial \mathbf{C}} - \lambda \mathbf{C}^{-1}$$

Here,  $\mathbf{C} = 2\mathbf{E} + \mathbf{I}$  is the right Cauchy–Green tensor and  $\lambda$  is a Lagrange multiplier to enforce incompressibility.  $\psi_{el}$  is the elastic strain energy function, and in the Lee–Sacks model it is defined as

$$\psi_{el} = \frac{c_0}{2}(I_1 - 3) + \frac{c_1}{2}(we^{c_2(I_1-3)^2} + (1-w)e^{c_3(I_4-3)^2} - 1)$$

where  $c_0$ ,  $c_1$ ,  $c_2$ , and  $c_3$  are material parameters and  $w \in [0, 1]$  represents the material’s level of anisotropy.  $I_1 = \text{tr}\mathbf{C}$  and  $I_4 = \mathbf{m} \cdot \mathbf{C}\mathbf{m}$ , with  $\mathbf{m}$  being a unit vector that defines the collagen fiber direction in the material. Valve tissue is typically anisotropic due to orientation of collagen fibers in the tissue, and this anisotropy can easily be handled by Kirchoff–Love shell formulations.<sup>[28,29]</sup> Wu *et al.*, however, suggests that the anisotropy of the leaflets has a relatively small effect for large deformations compared to the sizes of the leaflets, such as those explored in this work evaluating closure of the entire TV. Further, obtaining collagen fiber orientation data is a difficult topic outside the scope of this work; see Jett *et al.*<sup>[30]</sup> for methods which can be used to obtain these data. Future extensions for this modeling pipeline could include such anisotropy studies, but for this work we assume  $w = 1.0$ , reducing the Lee–Sacks model to the simpler isotropic Fung-type material model. For the material parameters, we select  $c_0 = 10$  kPa,  $c_1 = 0.209$  kPa, and  $c_2 = 9.046$ , obtained from Table 2 in Stevanella *et al.*, and use a leaflet mass density of  $1 \text{ g/cm}^3$ .

We model the chordae tendineae using the St. Venant–Kirchhoff material model. As chordae are stretched, their collagen fibers transition from slacked to stretched, contributing no tensile stiffness in the initial state. Once a chorda is stretched, most collagen fibers begin contributing to the stiffness, leading to post-transition stiffness several orders of magnitude larger than the pre-transition stiffness. While inadequate for modeling biological soft tissue like the TV leaflet, the St. Venant–Kirchhoff model is suitable for chordae tendineae if the assumption is made that the cable’s



reference configuration has been stretched beyond the pre-transition state to where the material exhibits a more linear stress-strain behavior. For this analysis, we assume the reference configuration of the chordae includes strain up to the transition point, and simply use Young's modulus to determine stiffness for the chordae cable models. We select a post-transition stiffness  $E^{ca} = 4 \times 10^8 \text{ dyn/cm}^2$ , as used by Kamensky *et al.*<sup>[15]</sup> to reflect the moderately higher stiffness of tricuspid chordae as compared to mitral chordae.

For boundary conditions we pin the annulus by fixing the annulus control points. Chordae connection to the papillary muscles are subject to strongly-enforced homogeneous Dirichlet boundary conditions. We apply a pressure load gradually increasing over a time step of 0.01 s to 25 mmHg, which is a typical right ventricular systolic pressure.<sup>[31]</sup> These boundary conditions are applied to the model using IGA in the form of analysis code written in FORTRAN using the contact formulation found in Kamensky *et al.*<sup>[15]</sup> Figure 5.1 depicts a fully-closed TV model after loading has been applied and steady state is reached. Contact between leaflets is highlighted in red.

## 5.2 Optimization

IGA limits the amount of manual input required for analysis. This allows for the possibility of optimizing the valve configuration. When TR occurs, the preferred treatment is repair of the valve; however, sometimes valve repair is not an option, and valve replacement is required using a prosthetic valve. One method for evaluating the effectiveness of a valve is its coaptation area, which is the contact area between its leaflets. Higher coaptation areas correlate to lower the chances of regurgitation. Coaptation area has previously been used as a metric for evaluating the effectiveness of the aortic valve.<sup>[14]</sup>

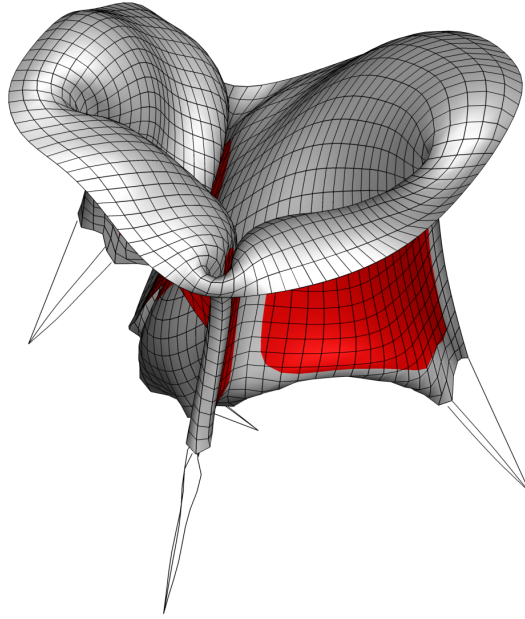


**FIG. 5.1** Closed TV configuration, with leaflet contact area highlighted in red.

For this reason, we use coaptation area of the TV model to evaluate its effectiveness as a prosthetic valve design.

For our optimization algorithm, we choose the genetic algorithm. Genetic algorithms are a common type of optimization algorithm which minimize an objective function. The genetic algorithm initially generates a population of parameter sets within a set of user-defined bounds. It then evaluates the fitness score of each population member using the objective function. It uses the sets with better fitness values as parents for the next generation by combining their parameters to make new parameter sets. This process approaches the local minimum for the objective function as each generation continues. A few parameter sets, called mutations, are randomized each generation. This allows the algorithm to search outside the area approaching a local minimum to find a global minimum, a key reason for choosing the genetic algorithm for optimization. Another key advantage of the genetic algorithm is that it can handle optimization using both integer and non-integer input parameters. This is important because some input model parameters, such as the leaflet and commissure heights, are non-

integers, while other parameters are integers, such as the number of chordae tendineae in each group.

The genetic algorithm requires two major components to function: a set of parameters to optimize with upper and lower bounds, and an objective function to minimize. We want to maximize coaptation area to limit regurgitation, but we want to design a more efficient prosthetic tricuspid valve, rather than just a larger one. For this reason, we use the simplified objective function of

$$F = - \frac{A_{\text{coaptation, deformed}}}{A_{\text{total, reference}}}$$

to validate our optimization framework. This is a ratio of the TV coaptation area in the deformed configuration, which is the quantity we wish to maximize, and the total TV area in the initial reference configuration, which is the quantity we control with the input parameters. Since the genetic algorithm tries to minimize the objective function, we make this ratio negative. The set of parameters to optimize is the set of parameters used as an input for the TV model. The leaflet and commissure height limits are set at two standard deviations above and below the limits measured by Stevanella *et al.*<sup>[2]</sup> This allows for significant variation in model geometry when searching for optimal designs, but keeps the search area restricted to mostly feasible dimensions.

Figure 5.2 gives an overview of the framework used for optimization. The initial selected parameters are fed into the Grasshopper model, near-instantaneously generating the model geometry. Analysis is then performed directly on the generated model using IGA, using FORTRAN code to apply the conditions described in Section 5.1. Once analysis has converged and the valve is closed, its coaptation area is calculated as an output of the analysis code and its input parameters, area, and coaptation area are output to a log file. An in-house optimization code running in MATLAB detects the

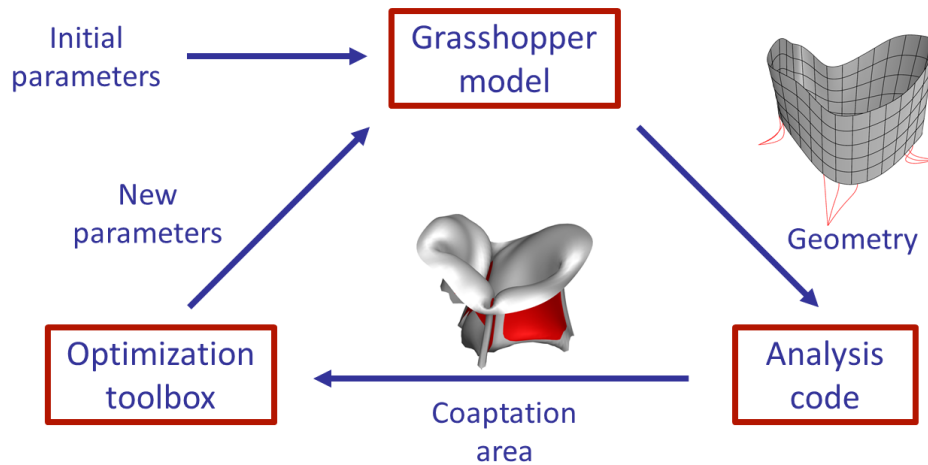


FIG. 5.2 Optimization framework

change to this log file and reads in these outputs and parameters. It then uses the genetic algorithm to generate a new set of parameters based on the previous results and output those to the model's input parameter file. These new parameters again create a new TV model near-instantaneously, and a new analysis for valve closure begins. This cycle continues until a stopping condition is met; in the following case, a specific number of iterations was used, but to find a true global minimum a stopping condition such as a threshold for increasingly small changes in objective function should be used. An overview of the entire optimization pipeline is shown in Fig. 5.6.

Figure 5.3 shows the objective function value over thirty steps of optimization. While most parameter configurations resulted in an objective function value of approximately -0.06, three configurations had objective function values near zero, meaning that they had very poor closure. These high objective function values indicate either infeasible parameter combinations or a valve design which would likely have significant regurgitation. Of interest are the six parameter combinations which had a much lower objective function value, less than -0.08, indicating these configurations had improved TV closure.

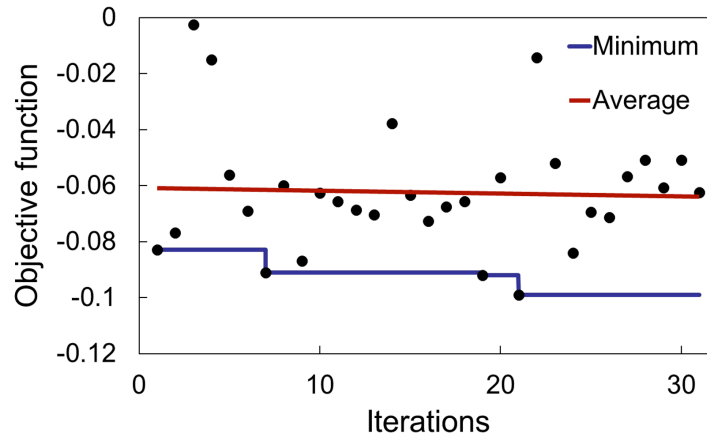
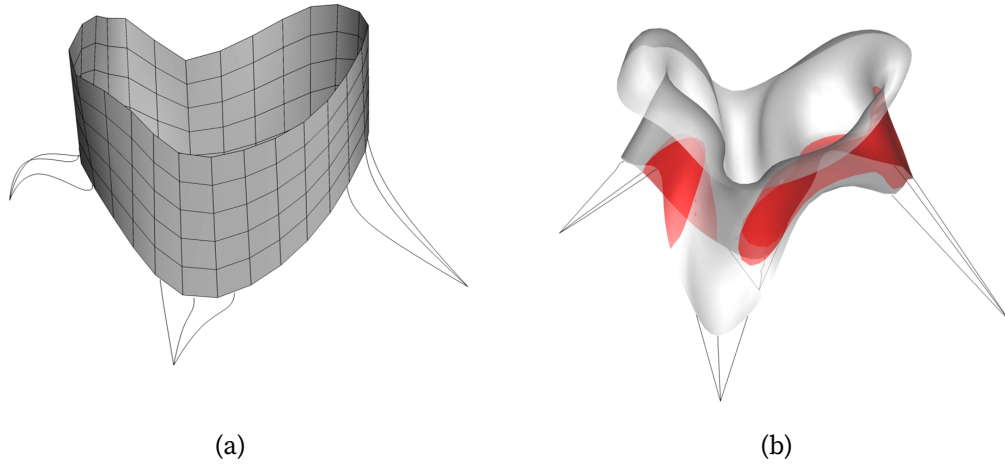


FIG. 5.3 Objective function value as optimization continues.

The smallest objective function found from these iterations was -0.9896, resulting from a coaptation area of  $1.11 \text{ cm}^2$  and a total initial area of  $11.26 \text{ cm}^2$ . The model for this parameter configuration is shown in Fig. 5.4, for both the initial model and the closed TV shape. Since coaptation area is the quantity of interest, the valve's coaptation area is highlighted in red, exhibiting good contact across the entire valve near the free edge. Fig. 5.5 shows the maximum in-plane Green-Lagrange strain (MIPE) of the valve. We see that the greatest tissue deformation is seen near the free edge, while the annulus has very limited deformation near the fixed boundary conditions.

## 5.3 Patient Education

The expanding availability of rapid prototyping in recent years has opened up new ways to translate digital ideas into the physical space. One way we can use this technology is in educating patients about issues with their atrioventricular heart valves. By placing 3D printing technology at the end of our modeling pipeline, we can give clinicians a physical representation of a patient's heart valve that they can use as a tool for explaining repair procedures.



**FIG. 5.4** Best TV configuration, (a) undeformed and (b) deformed with coaptation highlighted in red.

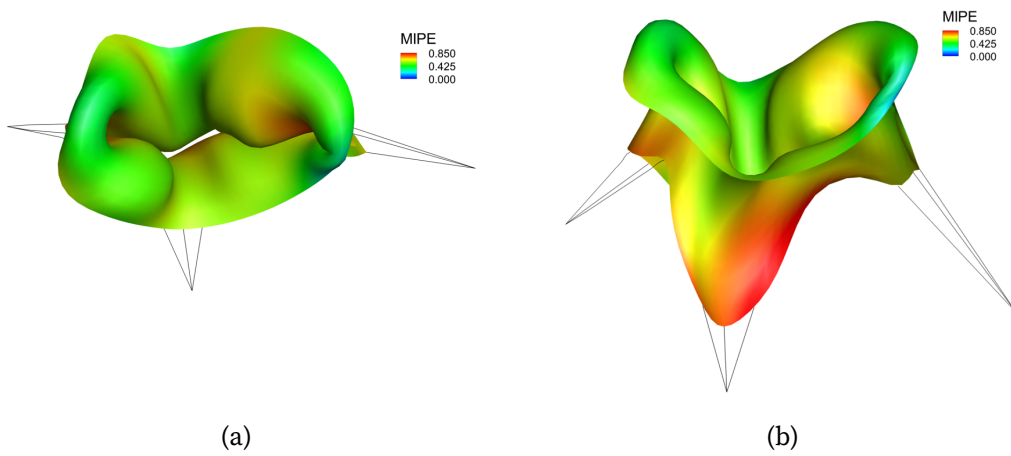


**FIG. 5.5** Best TV configuration with maximum in-plane Green-Lagrange strain (MIPE), (a) top view and (b) side view.

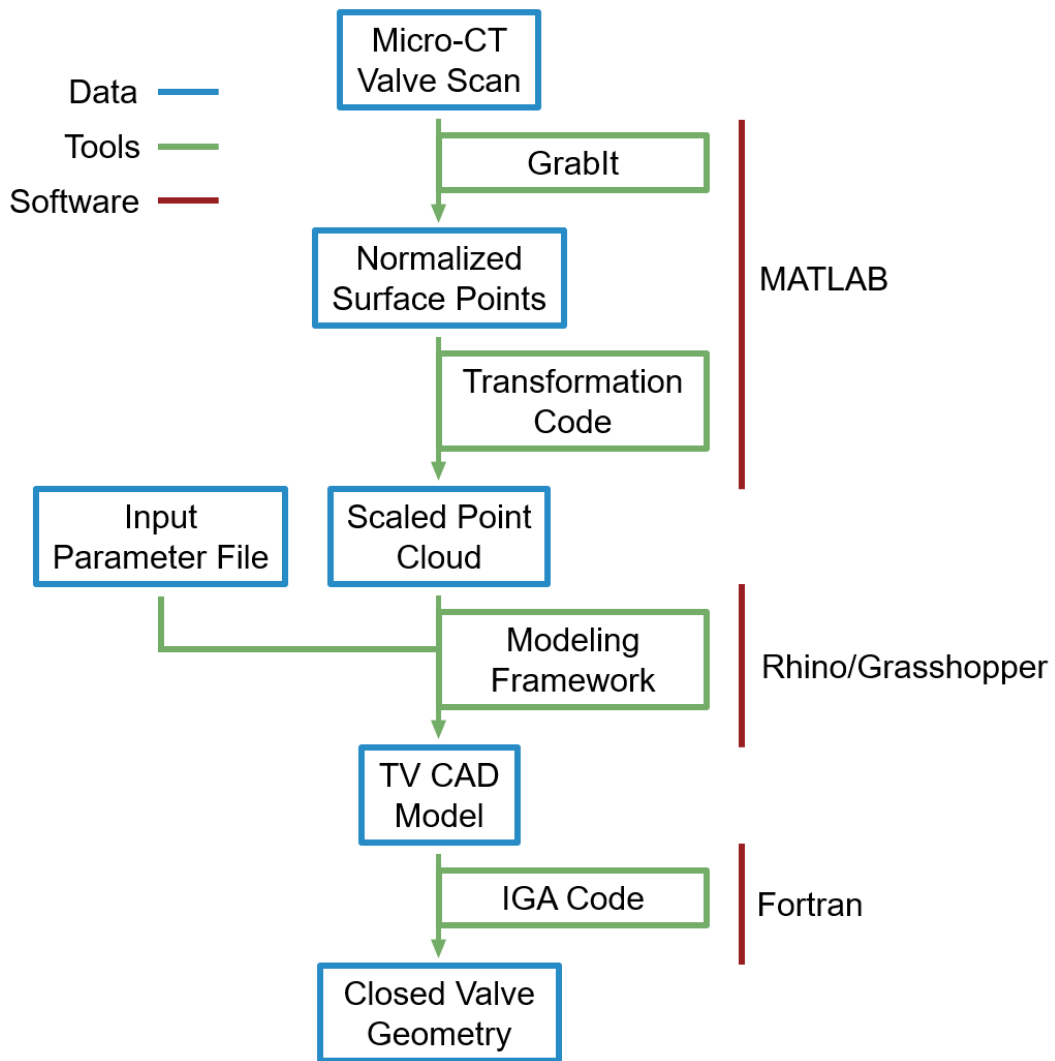
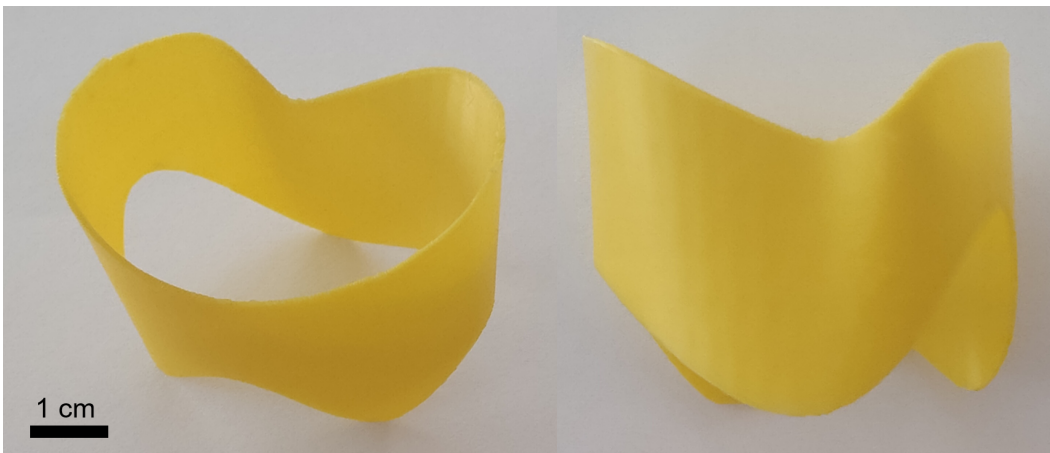


FIG. 5.6 An overview of the full optimization pipeline.

A major draw of this modeling pipeline is having a streamlined process that can be placed in the clinical setting. The foundation of the process is starting with clinical image scans of a patient's heart valve. Through the pipeline, a 3D model geometry is created in Grasshopper. It is then a simple process to 3D print the generated model, which is demonstrated here. The model is created by the code in the Grasshopper plugin, but is built within the Rhinoceros 3D software. We then “bake” the model, an option which changes the model from a preview created by Grasshopper into a solid object in Rhino. Once the model is baked, it can be exported from Rhino into one of many 3D model formats. For the purpose of 3D printing, we choose to export our model as a stereolithography (.stl) file. From there, we import the file into a slicer software such as Ultimaker Cura. In the slicer software chosen, the file can be scaled to the desired dimensions; larger scaled objects are able to show more detail, but will take more time to print. Once sliced, the model is able to be printed on any commercially-available 3D printer, creating a physical patient-specific tricuspid valve model.



**FIG. 5.7** 3D-printed TV leaflet surface.

Figure 5.7 shows an example valve model printed using the process described above. Polylactic acid (PLA), a thermoplastic monomer popular for 3D printing due to its ease of printing, was used for this example. The model in its initial configuration is relatively simple and quick to print (1hr), requir-



ing no supports and achieving a high final print quality. Figure 5.8 depicts a printed example of a closed valve configuration, after loading conditions have been applied and the solution has converged. This print is significantly more complex to print, requiring supports to be printed for the many overhangs, increasing the print time (1h 40m). In addition, post processing was required to remove the supports once printing was complete. The surface quality of the print is lower than the open valve configuration, but it still achieves its goal of providing a physical model showing proper closure of the TV. For patients with functional TR, this pipeline could be used to provide physical models to the patient demonstrating their own TV geometry before and after surgical intervention, improving understanding of the procedure.

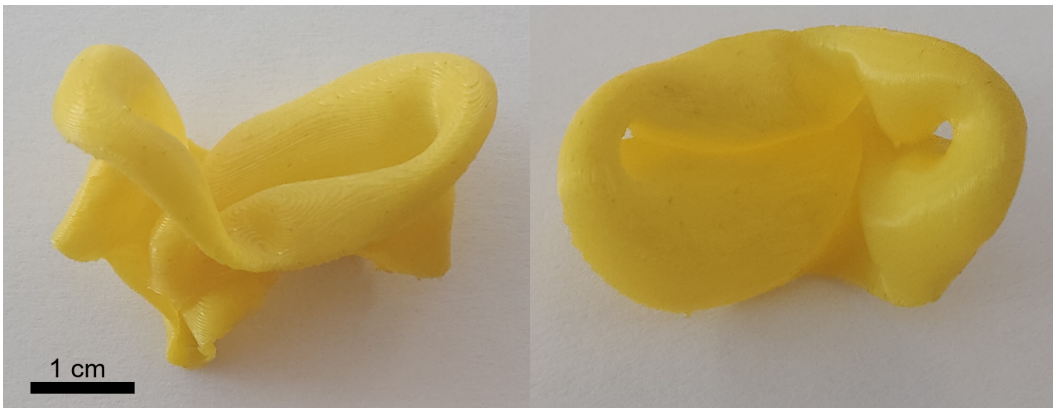


**FIG. 5.8** 3D-printed TV closed leaflet surface.

## 6 CONCLUSIONS AND FUTURE WORK

6.1	Conclusions . . . . .	<b>60</b>
6.1.1	Geometry Modeling Pipeline . . . . .	61
6.1.2	Modeling Applications . . . . .	61
6.2	Recommendations for Future Research . . . . .	<b>61</b>
6.2.1	Additional patient-specific parameters . . . . .	61
6.2.2	Streamlining valve segmentation . . . . .	62
6.2.3	Dynamic modeling conditions . . . . .	62
6.2.4	Alternate optimization methods . . . . .	63

### 6.1 Conclusions

This research developed a geometry modeling pipeline for the tricuspid heart valve. It aims to provide the next step towards seamless patient-specific heart valve modeling by combining patient heart data with a flexible geometry model that can immediately be used for analysis without an intermediate meshing step. The model is adaptable and open to many applications and improvements. Two such applications, prosthetic valve optimization and patient education, were explored in this work. Potential improvements to the pipeline are listed at the end of this chapter.

### **6.1.1 Geometry Modeling Pipeline**

The developed pipeline can be broadly divided into two major parts. The first part used patient  $\mu$ CT image data with manual surface digitization to create a 3-dimensional point cloud surface of the closed TV, with points labeled by leaflet and the annulus points identified. The point cloud was then imported into the second component of the pipeline, a model created in Rhinoceros 3D using the Grasshopper visual programming plugin. The model combined the input point cloud annulus with a set of input parameters derived from literature to create a CAD surface of the open TV using NURBS. Chordae tendineae were also defined linking the free edge of the leaflets to fixed points representing the papillary muscles in the heart to complete the model.

### **6.1.2 Modeling Applications**

We used the modeling pipeline described in Section 6.1.1 to model four different tricuspid valves from patient data. Additionally, we demonstrated the flexibility of the TV model by demonstrating the variety of ways in which its shape can be altered, with different chordae groupings, attachment positions, and differences in leaflet and commissure heights. We also showed how the model can be adapted to the similar mitral valve structure.

## **6.2 Recommendations for Future Research**

We conclude by suggesting the following topics for future research studies.

### **6.2.1 Additional patient-specific parameters**

One way the model can be made more relevant to the clinical setting is in improving the patient-specific aspect of its approach. Currently, the model

draws annulus dimensions from segmented data of an excised heart valve. However, the dimensions of the leaflets, specifically the leaflet and commissure heights, are drawn from literature rather than patient data. If patient-specific leaflet dimensions can also be reliably extracted from scan data, these can easily be used in place of values drawn from literature to create a model that more accurately reflects a specific patient's TV, making it easier to identify and treat diseased conditions for that patient.

### **6.2.2 Streamlining valve segmentation**

The current pipeline has a high time cost necessary to produce the accurately-segmented TV surfaces that form the model's foundation. Manual segmentation used for the data sets in this research means there is significant delay between initial data collection and the final model. Automating the segmentation process is the next step to improving the pipeline using the relatively high quality and contrast of  $\mu$ CT image data. This would increase sample sizes feasible for working with the pipeline, improving the quality of future studies. More challenging will be automating segmentation for *in vivo* imaging modalities that typically have a lower resolution, but working toward this goal will create an almost real-time model that can be used in a clinical setting.

### **6.2.3 Dynamic modeling conditions**

A limitation of the present computational model is its use of fixed boundary conditions for the annulus and chordae tendineae attachments. The TV annulus is a dynamic structure that dilates and contracts during systole and diastole. Likewise, the papillary muscles are in constant motion during the beating of the heart. Adding annular motion as prescribed boundary conditions would improve the model's ability to simulate true closure of the valve. Improvements to *in vivo* clinical imaging modalities would allow for

tracking of patient-specific dynamic annulus and papillary muscle data that could then be added to the modeling pipeline and allow for exploration of more complex heart conditions.

#### **6.2.4 Alternate optimization methods**

At this time, model optimization is still computationally expensive; however, differential evolution optimization is one alternative to the current genetic algorithm that could be used to decrease this processing cost.<sup>[32,33]</sup> Like the genetic algorithm, differential evolution algorithms are designed to mimic evolution, and have the ability to search for a global minimum without getting trapped in a local minimum. They have the advantage of being relatively quick to converge and could thus be used to decrease long computation times present with the genetic optimization method used in this study, allowing for a wider exploration of the solution space or increased parameter complexity within the same computation time frame.

## REFERENCES

- [1] G. Dreyfus, P. Corbi, K. Chan, and T. Bahrami, “Secondary tricuspid regurgitation or dilatation: Which should be the criteria for surgical repair?” *Annals of Thoracic Surgery*, vol. 79, no. 1, pp. 127–132, 2005 (cit. on pp. 2, 15).
- [2] M. Stevanella, E. Votta, M. Lemma, C. Antona, and A. Redaelli, “Finite element modelling of the tricuspid valve: A preliminary study,” *Medical Engineering and Physics*, vol. 32, pp. 1213–1223, 2010 (cit. on pp. 2, 6–11, 13, 19, 26, 28, 29, 33, 41, 42, 50, 53).
- [3] C.-H. Lee, D. W. Laurence, C. J. Ross, K. E. Kramer, A. R. Babu, *et al.*, “Mechanics of the tricuspid valve—from clinical diagnosis/treatment, in-vivo and in-vitro investigations, to patient-specific biomechanical modeling,” *Bioengineering*, vol. 6, p. 47, 2019 (cit. on pp. 5, 14, 17).
- [4] K. A. Khoiy and R. Amini, “On the biaxial mechanical response of porcine tricuspid valve leaflets,” *Journal of Biomechanical Engineering*, vol. 138, 2016 (cit. on p. 6).
- [5] M. Hiro, J. Jouan, M. Pagel, E. Lansac, H.-S. Lim, *et al.*, “Sonometric study of the normal tricuspid valve annulus in sheep,” *The Journal of Heart Valve Disease*, vol. 13, pp. 452–60, 2004 (cit. on pp. 6, 8–10, 28).
- [6] J. Jouan, M. R. Pagel, M. E. Hiro, K. H. Lim, E. Lansac, *et al.*, “Further information from a sonometric study of the normal tricuspid valve annulus in sheep: Geometric changes during the cardiac cycle,” *The*

- Journal of Heart Valve Disease*, vol. 16, no. 5, pp. 511–518, 2007 (cit. on p. 6).
- [7] S. Fukuda, G. Saracino, Y. Matsumura, M. Daimon, H. Tran, *et al.*, “Three-dimensional geometry of the tricuspid annulus in healthy subjects and in patients with functional tricuspid regurgitation: a real-time, 3-dimensional echocardiographic study,” *Circulation*, vol. 114, pp. I-492–I-498, 2006 (cit. on pp. 6, 8).
- [8] M. D. Silver, J. H. C. Lam, N. Ranganathan, and E. D. Wigle, “Morphology of the human tricuspid valve,” *Circulation*, vol. 43, no. 3, pp. 333–348, 1971 (cit. on p. 7).
- [9] A. Pokutta-Paskaleva, F. Sulejmani, M. DelRocini, and W. Sun, “Comparative mechanical, morphological, and microstructural characterization of porcine mitral and tricuspid leaflets and chordae tendineae,” *Acta Biomaterialia*, vol. 85, pp. 241–252, 2019 (cit. on pp. 7, 9).
- [10] A. Aversa and E. Careddu, “Image-based analysis of tricuspid valve biomechanics: Towards a novel approach integrating in-vitro 3D-echocardiography and finite element modelling,” Master’s Thesis, Politecnico di Milano, Milan, Italy, 2017 (cit. on pp. 9, 10, 28).
- [11] F. Kong, T. Pham, C. Martin, R. McKay, C. Primiano, *et al.*, “Finite element analysis of tricuspid valve deformation from multi-slice computed tomography images,” *Annals of Biomedical Engineering*, pp. 1–16, 2018 (cit. on pp. 11, 19).
- [12] S. Singh-Gryzbon, V. Sadri, M. Toma, E. Pierce, Z. Wei, *et al.*, “Development of a computational method for simulating tricuspid valve dynamics,” *Annals of Biomedical Engineering*, vol. 47, pp. 1422–1434, 2019 (cit. on pp. 11, 12, 19, 28, 29).
- [13] A. M. Pouch, A. H. Aly, A. Lasso, A. V. Nguyen, A. B. Scanlan, *et al.*, “Image segmentation and modeling of the pediatric tricuspid valve in

- hypoplastic left heart syndrome,” *Functional Imaging and Modelling of the Heart*, pp. 95–105, 2017 (cit. on pp. 11, 13).
- [14] F. Xu, S. Morganti, R. Zakerzadeh, D. Kamensky, F. Auricchio, *et al.*, “A framework for designing patient-specific bioprosthetic heart valves using immersogeometric fluid–structure interaction analysis,” *International Journal for Numerical Methods in Biomedical Engineering*, vol. 34, no. 4, 2018 (cit. on pp. 13, 14, 51).
- [15] D. Kamensky, F. Xu, C.-H. Lee, J. Yan, Y. Bazilevs, *et al.*, “A contact formulation based on a volumetric potential: Application to isogeometric simulations of atrioventricular valves,” *Computer Methods in Applied Mechanics and Engineering*, vol. 330, pp. 522–546, 2018 (cit. on pp. 13, 14, 49, 51).
- [16] A. J. Herrema, N. M. Wiese, C. N. Darling, B. Ganapathysubramanian, A. Krishnamurthy, *et al.*, “A framework for parametric design optimization using isogeometric analysis,” *Computer methods in applied mechanics and engineering*, vol. 316, pp. 944–965, 2017 (cit. on p. 14).
- [17] P. C. Come and M. F. Riley, “Tricuspid annular dilatation and failure of tricuspid leaflet coaptation in tricuspid regurgitation,” *The American Journal of Cardiology*, vol. 55, no. 5, pp. 599–601, 1985 (cit. on p. 14).
- [18] C. Besler, C. Meduri, and P. Lurz, “Transcatheter treatment of functional tricuspid regurgitation using the Trialign device,” *Interventional Cardiology Review*, vol. 13, p. 1, Jan. 2017 (cit. on p. 16).
- [19] O. Stuge and J. Liddicoat, “Emerging opportunities for cardiac surgeons within structural heart disease,” *The Journal of Thoracic and Cardiovascular Surgery*, vol. 132, no. 6, pp. 1258–1261, 2006 (cit. on p. 15).
- [20] N. S. Braunwald, J. R. Jr., and A. G. Morrow, “Conservative management of tricuspid regurgitation in patients undergoing mitral valve



- replacement,” *Circulation*, vol. 35, no. 4, pp. I-63–I-69, 1967 (cit. on p. 15).
- [21] A. Carpentier, “A new reconstructive operation for correction of mitral and tricuspid insufficiency,” *Journal of Thoracic Cardiovascular Surgery*, vol. 61, pp. 1–13, 1971 (cit. on p. 16).
- [22] N. D. de Vega, G. de Rábago, L. Castellón, T. Moreno, and J. Azpitarte, “A new tricuspid repair. short-term clinical results in 23 cases,” *The Journal of Cardiovascular Surgery*, vol. 14, pp. 384–386, 1973 (cit. on p. 16).
- [23] F. Milla, J. G. Castillo, R. Varghese, J. Chikwe, A. C. Anyanwu, *et al.*, “Rationale and initial experience with the Tri-Ad Adams tricuspid annuloplasty ring,” *Journal of Thoracic Cardiovascular Surgery*, vol. 143, pp. 71–73, 2012 (cit. on p. 18).
- [24] E. M. Spinner, P. Shannon, D. Buice, J. H. Jimenez, E. Veledar, *et al.*, “In vitro characterization of the mechanisms responsible for functional tricuspid regurgitation,” *Circulation*, vol. 124, no. 8, pp. 920–929, 2011 (cit. on p. 19).
- [25] T. M. Joudinaud, E. M. Flecher, and C. M. G. Duran, “Functional terminology for the tricuspid valve,” *The Journal of Heart Valve Disease*, vol. 15, no. 3, pp. 382–388, 2006 (cit. on p. 26).
- [26] C.-H. Lee, R. Amini, R. C. Gorman, J. H. G. 3rd, and M. S. Sacks, “An inverse modeling approach for stress estimation in mitral valve anterior leaflet valvuloplasty for in-vivo valvular biomaterial assessment,” *Journal of Biomechanics*, vol. 47, no. 9, pp. 2055–2063, 2000 (cit. on p. 49).
- [27] M. C. Wu, R. Zakerzadeh, D. Kamensky, J. Kiendl, M. S. Sacks, *et al.*, “An anisotropic constitutive model for immersogeometric fluid–structure interaction analysis of bioprosthetic heart valves,” *Journal of Biomechanics*, vol. 74, pp. 23–31, 2018 (cit. on pp. 49, 50).

- [28] A. B. Tepole, H. Kabaria, K.-U. Bletzinger, and E. Kuhl, “Isogeometric Kirchhoff–Love shell formulations for biological membranes,” *Computer Methods in Applied Mechanics and Engineering*, vol. 293, pp. 328–347, 2015 (cit. on p. 50).
- [29] F. Roohbakhshan and R. A. Sauer, “Efficient isogeometric thin shell formulations for soft biological materials,” *Biomechanics and Modeling in Mechanobiology*, vol. 16, no. 5, pp. 1569–1597, 2017 (cit. on p. 50).
- [30] S. V. Jett, L. T. Hudson, R. Baumwart, B. N. Bohnstedt, A. Mir, *et al.*, “Integration of polarized spatial frequency domain imaging (pSFDI) with a biaxial mechanical testing system for quantification of load-dependent collagen architecture in soft collagenous tissues,” *Acta Biomaterialia*, vol. 102, pp. 149–168, 2020 (cit. on p. 50).
- [31] A. Aessopos, D. Farmakis, H. Taktikou, and D. Loukopoulos, “Doppler-Determined Peak Systolic Tricuspid Pressure Gradient in Persons with Normal Pulmonary Function and Tricuspid Regurgitation,” *Journal of the American Society of Echocardiography*, vol. 13, no. 7, pp. 645–649, 2000 (cit. on p. 51).
- [32] F. Neri and V. Tirronen, “Recent advances in differential evolution: a survey and experimental analysis,” *Artificial Intelligence Review*, vol. 33, pp. 61–106, Feb. 2010 (cit. on p. 63).
- [33] S. Das, S. S. Mullick, and P. Suganthan, “Recent advances in differential evolution -- An updated survey,” *Swarm and Evolutionary Computation*, vol. 27, pp. 1–30, 2016 (cit. on p. 63).